



HAL
open science

Permittivity and electrical resistivity measurements and estimations during the recovery of DNAPL in saturated porous media: 2D tank experiments

Stéfan Colombano, Hossein Davarzani, E. D. van Hullebusch, D. Huguenot, Dominique Guyonnet, Jacques Deparis, Ioannis Ignatiadis

► To cite this version:

Stéfan Colombano, Hossein Davarzani, E. D. van Hullebusch, D. Huguenot, Dominique Guyonnet, et al.. Permittivity and electrical resistivity measurements and estimations during the recovery of DNAPL in saturated porous media: 2D tank experiments. *Journal of Applied Geophysics*, 2021, 191, pp.2355-2377. 10.1016/j.jappgeo.2021.104359 . insu-03590025

HAL Id: insu-03590025

<https://insu.hal.science/insu-03590025>

Submitted on 24 May 2023

HAL is a multi-disciplinary open access archive for the deposit and dissemination of scientific research documents, whether they are published or not. The documents may come from teaching and research institutions in France or abroad, or from public or private research centers.

L'archive ouverte pluridisciplinaire **HAL**, est destinée au dépôt et à la diffusion de documents scientifiques de niveau recherche, publiés ou non, émanant des établissements d'enseignement et de recherche français ou étrangers, des laboratoires publics ou privés.



Distributed under a Creative Commons Attribution - NonCommercial 4.0 International License

1 Permittivity and electrical resistivity measurements and estimations during the
2 recovery of DNAPL in saturated porous media: 2D tank experiments

3 S. Colombano^{1*}, H. Davarzani¹, E.D van Hullebusch², D. Huguenot³, D. Guyonnet¹, J. Deparis¹,
4 I. Ignatiadis¹

5
6 ¹ BRGM (French Geological Survey), 45060 Orléans, France

7 ² Université de Paris, Institut de Physique du Globe de Paris, CNRS, F-75005 Paris, France

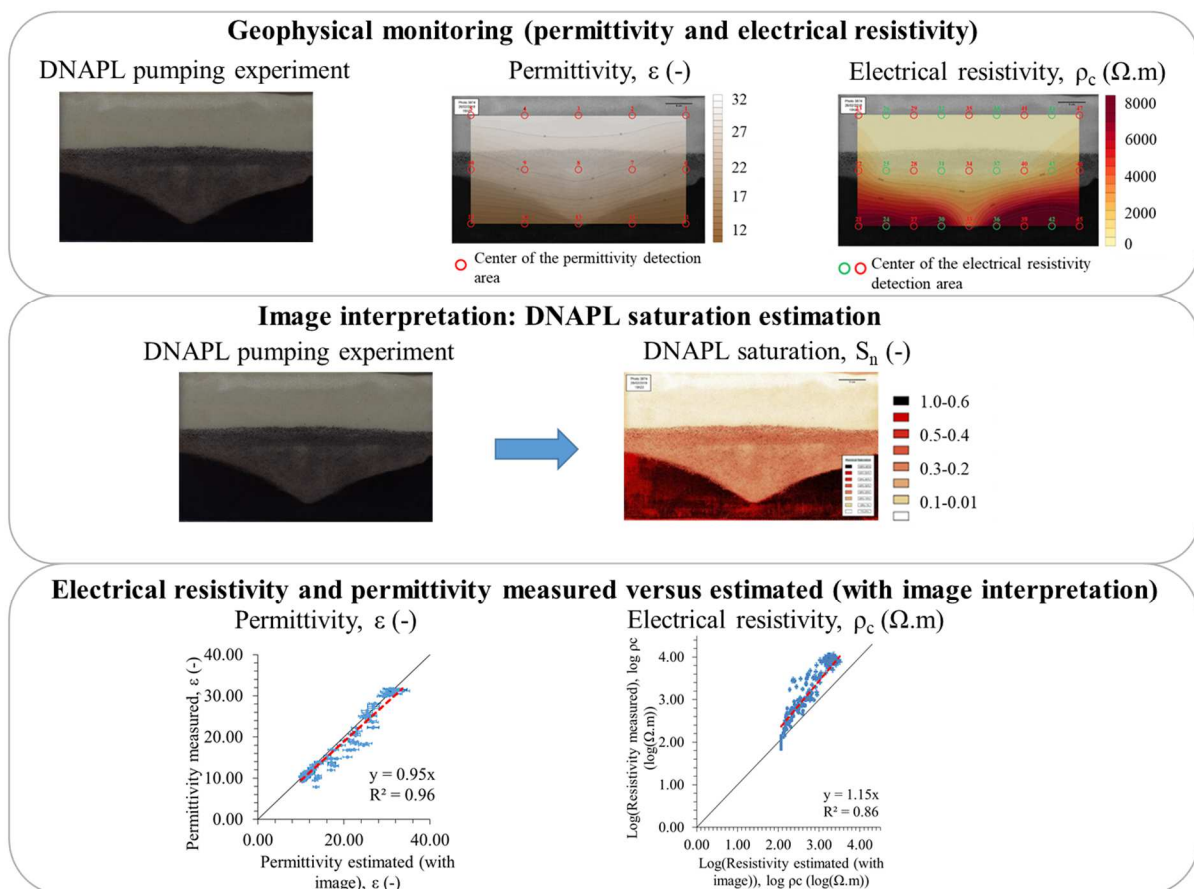
8 ³ Laboratoire Géomatériaux et Environnement, Université Gustave Eiffel, 77454 Marne-la-Vallée,
9 France

10

11 *corresponding author: Stéfan Colombano: s.colombano@brgm.fr

12

13 **Graphical abstract**



14

15 **Highlights**

- 16 • 2D tank experiments were performed to estimate DNAPL recovery
- 17 • DNAPL recovery was monitored with permittivity and electrical resistivity measurements
- 18 • DNAPL saturation estimation with permittivity is very accurate
- 19 • Electrical resistivity monitoring allows less accurate estimation of DNAPL saturation

20

21 **Abstract**

22 Pumping experiments were performed in a 2D tank in order to estimate the recovery yield and rate
23 of pure heavy chlorinated organic compounds (DNAPL; dense non-aqueous phase liquids). Several
24 operating configurations were considered: permeability of the saturated zone, pumping flow rates,
25 addition of surfactant (to reduce capillary effects), and thermal treatment (to reduce DNAPL
26 viscosity). The experiments were monitored with permittivity (ϵ) and electrical resistivity (ρ)
27 measurements. The experiments were also monitored with photography allowing, based on image
28 interpretation, to accurately convert optical densities into water saturations (S_w) and to validate the
29 geophysical data collected. Average S_w were determined in all detection areas from permittivities and
30 electrical resistivities. These average S_w were used to calculate theoretical permittivities using the
31 complex refractive index model (CRIM) and theoretical electrical resistivities using Archie's law. We
32 found a good correlation between measured permittivities and the estimated permittivities with image.
33 Conversely, the correlation was less accurate between measured and estimated electrical resistivities
34 except for low electrical resistivities (*i.e.* high S_w). It is therefore not possible to accurately quantify
35 water saturations using electrical resistivity monitoring alone. However, the accuracy is sufficient
36 (especially for high values of S_w) to highlight differences between the three considered treatment
37 technologies (*i.e.* without enhancement, with chemical and/or thermal enhancements). A combination
38 of monitored electrical resistivity (which provides an integrated vision of the cone of depression) and
39 monitored permittivity (which provides accurate but spatially limited information), and imaging
40 allows a more accurate calibration of the relationship between resistivities and S_w and quantification of
41 remediation rates and yields.

42

43 **Keywords**

44 Dense non-aqueous phase liquids, two-phase flow, porous media, free product recovery, electrical
45 resistivity monitoring, permittivity monitoring.

46 1. Introduction

47 Chlorinated Organic Compounds (COCs) are particularly persistent and toxic pollutants that may
48 significantly contaminate different environmental media (soil, indoor air and groundwater [NIEHS
49 (2015); IARC (2018); Arp and Hale (2019)], over very long periods of time. These compounds have
50 been produced in large quantities since the middle of the 20th century mostly as solvents, pesticides,
51 electrical insulators [Cohen and Mercer (1993); Kueper et al. (2003)]. COCs are very hydrophobic and
52 are denser than water. In the event of chronic or accidental contamination, COCs infiltrate into the
53 vadose and saturated zones down to the substratum to form DNAPL (dense non-aqueous phase liquid)
54 pools [Cohen and Mercer (1993); Kueper et al. (2003)]. The recovery of DNAPL free-phase (mobile)
55 product is usually performed by implementing “pump and treat” methods. However, these methods are
56 not very efficient and commonly last for many years [ITRC (2002); Falta et al. (2005b); McGuire
57 et al. (2006)]. Also, this remediation technology does not allow a homogeneous recovery of the
58 DNAPL. Thus, it is essential to better: i. spatialize the residual saturations of DNAPL; and ii. monitor
59 the applied remediation operation in order to implement additional remediation measures on “hot
60 spots” and thus improve recovery rates [Maire et al. (2018)]. Geophysical techniques can help to better
61 characterize these pollution sources [Power et al. (2014)].

62 Geophysical investigation, used to characterize hydrocarbon contaminated sites, mainly relies on
63 the electrical properties of hydrocarbons because their presence may change some of the medium’s
64 physical properties, changes which can be detected using electrical measurements such as resistivity
65 measurements (classic or stationary and complex or transitory). These NAPLs have high electrical
66 resistivity and low dielectric constant (compared to water). They respectively decreases and increases
67 with increasing degradation, as does electric chargeability, *i.e.* the capacity to polarize, which is
68 significant and depends on their degradation state [Brown et al. (2003); Brown et al. (2004); Schmutz
69 et al. (2010); Smallwood (2012)]. Since the early 2000s, geophysical methods have been the subject of
70 intensive research to study environmental problems associated with hydrocarbons and to determine the
71 relationship between the geophysical signal and the contamination. Also, several electrical resistivity
72 monitoring experiments have been conducted to follow biogeochemical remediation in sites polluted
73 by chlorinated solvents and refined hydrocarbons [Nyquist et al. (1999); Power et al. (2014); Noel

74 et al. (2016a)]. Deng *et al.* (2017) have reported the importance of using laboratory tomography
75 measurements for electrical resistivity (classic) combined when possible with imaging techniques, to
76 improve the interpretation of resistivity measurements on sites polluted by NAPL and composed of
77 materials with varying permeabilities [Deng et al. (2017)].

78 This research aims to connect DNAPL saturations and electrical resistivity measurements.
79 Resistivity of soils depends of two different mechanisms: electrolytic and surface conduction (*i.e.*
80 presence of clay) [Revil (2012)]. Both terms are saturation-dependent. It should be noted that there is
81 no consensus regarding the interdependence of water saturation and the surface conductivity [Breede
82 et al. (2011); Laloy et al. (2011)]. Archie's law has been shown to provide relatively accurate estimates
83 of DNAPL [Kamona et al. (2003); Colombano et al. (2020); Iravani et al. (2020a)] in case of
84 electrolytic conduction.

85 One of the most commonly-used physical models of dielectric permittivity (ϵ), *i.e.*, the Complex
86 Refractive Index Model (CRIM), describes soil as a mixture of particles, water and air [Birchak et al.
87 (1974); Roth et al. (1990); Endres and Knight (1992)]. In the 1990s, studies aimed at connecting
88 DNAPL saturation (S_n) in saturated soils to the ϵ measured by time domain reflectometry (TDR)
89 probes [Redman et al. (1991); Redman and DeRyck (1994); Brewster et al. (1995)]. Perchloroethylene
90 samples, spiked at controlled saturations, were monitored by TDR. The measured permittivities allow
91 to estimate S_n in saturated porous media with good accuracy using the mixing models [Redman and
92 DeRyck (1994)]. Ajo-Franklin *et al.* (2004) obtained degrees of correlation higher than 97% using the
93 CRIM model in the case of trichloroethylene (TCE) in the saturated zone [Ajo-Franklin et al. (2004)].
94 Finally, Persson and Berndtsson (2002) showed that the mixing model used led to S_n estimation errors
95 up to 5% in the case of saturated sand “contaminated” by sunflower seed oil, synthetic motor oil and
96 paraffin [Persson and Berndtsson (2002)]. To minimize this error, Persson and Berndtsson coupled
97 TDR probes with the conductivity measurements.

98 Geophysical methods are complementary of intrusive investigation methods such as boreholes with
99 soil sample analyses, piezometers with water analyses, or soil-gas wells with gas analyses, and may
100 provide relatively spatially continuous information, where resolution is a function of electrodes
101 spacing and depth imaging [Chambers et al. (2004); Reynolds (2011)]. Several studies have

102 documented the potential of using electrical methods to monitor remediation of soil and groundwater
103 at both laboratory and field experimental scales [Sogade et al. (2006); Cardarelli and Di Filippo
104 (2009); Noel et al. (2016a); Noel et al. (2016b)]. Combining both electrical conductivity and dielectric
105 permittivity has been proven to be very effective for saturated soil characterization [Linde et al.
106 (2006); Brovelli and Cassiani (2011)].

107 The aim of this study was to demonstrate the accuracy of electrical resistivity and permittivity
108 monitoring methods as a mean to locate and estimate the saturation of DNAPL during laboratory
109 pumping experiments in a water-saturated porous medium. DNAPL recovery was performed by
110 pumping without enhancement as well as with chemical and thermal enhancements. Adding surfactant
111 aims to reduce capillary effects, whereas heating aims to reduce DNAPL viscosity, while both
112 methods aim to increase DNAPL recovery yield and rate during pumping. While the detailed results of
113 enhancement effects on DNAPL recovery are described elsewhere, this paper focuses on the
114 geophysical monitoring methods.

115

116 **2. Materials and methods**

117 The DNAPL pumping experiments in the 2D tank were performed with glass beads (GB) packing
118 of two distinct diameters (0.1 and 0.5 mm), different flow rates (50, 150, 220 mL.min⁻¹), without
119 thermal enhancement (at 20 °C), with chemical enhancements (with sodium dodecyl benzene
120 sulfonate, SDBS) at its critical micellar concentration (CMC, to avoid DNAPL dissolution) and/or
121 thermal enhancement at 50 °C (to avoid DNAPL volatilization). The use of glass beads helped avoid
122 potential artefact effects associated with porous medium heterogeneity, while the two different
123 diameters enabled to reproduce distinct hydraulic conductivities (1.30×10^{-10} m² and 6.73×10^{-12} m² for
124 0.5 mm GB and 0.1 mm GB, respectively).

125 The DNAPL used for the experiments was sampled at the Tavaux site (June 25, 2014), i.e., a large
126 chloralkali chemical plant located in the center-east of France. It was stored at 4 °C until use. DNAPL
127 was filtered just before its use (EMD Millipore, 0.45 µm). This DNAPL is a mixture of heavy
128 chlorinated organic compounds (weight percent; wt%): hexachlorobutadiene-HCBD (58%),
129 hexachloroethane-HCA (14%), perchloroethylene-PCE (8%), and pentachlorobenzene (3.5%), carbon

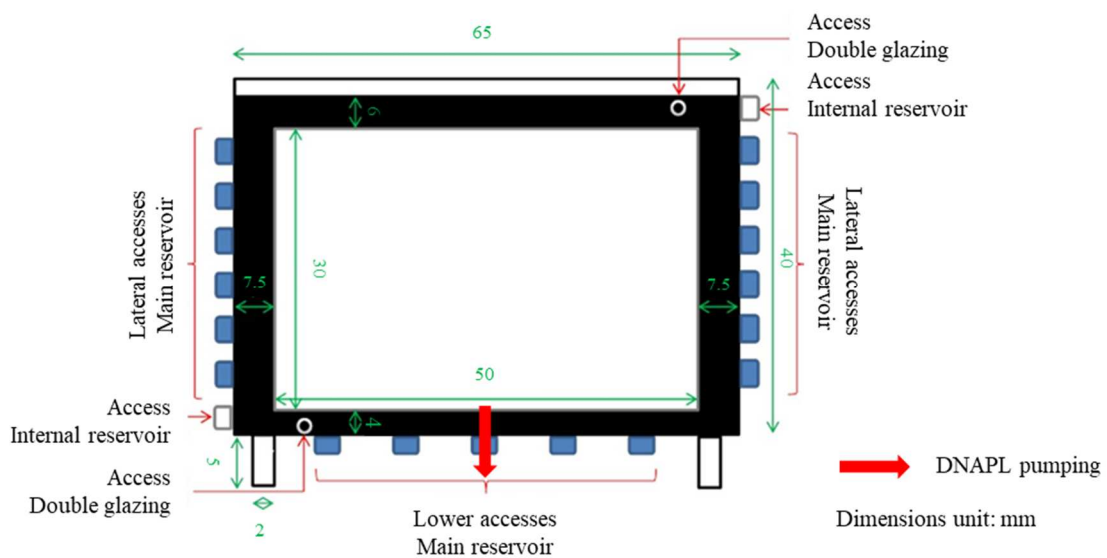
130 tetrachloride (4%), trichloroethylene-TCE (2%), hexachlorobenzene (1%) [Cazaux et al. (2014)]. The
 131 water used for all experiments was BRGM tap water. It was degassed using VWR Ultrasonic Cleaner
 132 (USC500D: 60 °C, 45 Hz, 60 min).

133

134 *2.1 DNAPL pumping experiments in the 2D tank and image interpretation*

135 The dimensions of the 2D tank, made of polyvinylidene difluoride (PVDF), were: L=50.00 cm,
 136 W=30.00 cm and H=7.00 cm (Figure 1).

137



138

139 Figure 1: Scheme of the experimental 2D tank, its main features and dimensions

140

141 Water was injected into the glass bead porous medium from the bottom of the 2D tank until it
 142 reached a height of 30.0 cm (at a flow rate of 0.05 mL.min⁻¹). Then, the DNAPL was injected to a
 143 height of 15.0 cm (in order to reach the irreducible saturation, S_{rw}) at a flow rate of 0.01 mL.min⁻¹. The central
 144 bottom access was used to pump the DNAPL during imbibition (red arrow in Figure 1). Several pipes
 145 were inserted inside each counter-channel to regulate the static level of air-water interface (at a height
 146 of 30.00 cm) and the static level of DNAPL-water interface (at a height of 15.00 cm) [Colombano
 147 et al. (2021)]. Two types of peristaltic pumps were used: Watson Marlow 205 and Watson Marlow
 148 530U; their flow rate ranges are 6.00×10^{-4} to 22.00 mL.min⁻¹ ($\pm 0.5\%$) and 4.00×10^{-3} to 2.40×10^3
 149

150 mL.min⁻¹
151 ($\pm 0.5\%$), respectively.

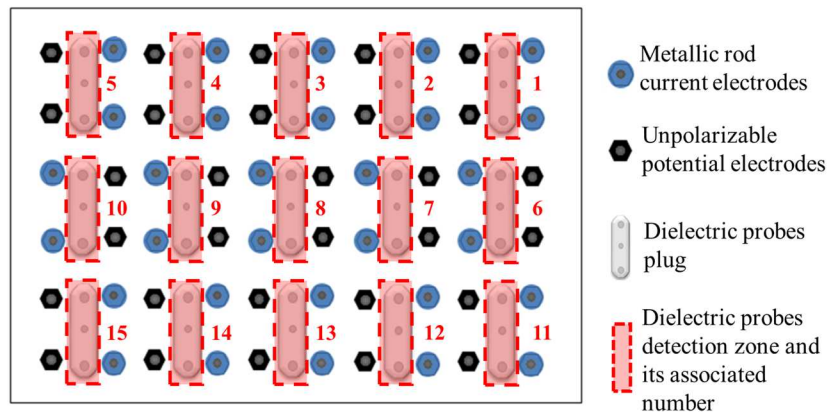
152 The experiments were monitored with photography allowing, based on image interpretation to
153 convert optical densities (OD) into S_w . The average S_w values were estimated in the detection areas of
154 the dielectric permittivity and electrical resistivity sensors (assuming a homogeneous medium). The
155 theoretical dielectric permittivity and electrical resistivity of the bulk (ϵ_{est} and $\rho_{c,est}$, respectively) were
156 estimated according to water and DNAPL saturations (using suitable mixing models) in these
157 detection areas. They were then compared to the permittivity and electrical resistivity measured (ϵ_{meas}
158 and $\rho_{c,meas}$, respectively).

159

160 2.2 Permittivity monitoring

161 Dielectric permittivities were monitored using capacitance/frequency domain technology (Decagon
162 Devices 5TE 40567) with a 70 MHz frequency. As well as permittivity (-), these dielectric probes
163 monitor temperature ($^{\circ}\text{C}$), and bulk electrical conductivity-EC (dS.m^{-1}). The probes were calibrated
164 and were connected to a Campbell Scientific CR1000 (4M) data logger and only used to acquire
165 temperature and permittivity data. Data acquisition frequency was 1 signal measurement per 30 s. In
166 total, 15 dielectric probes were arranged in the 2D tank. On the basis of the experiments conducted in
167 1D cells and 1D columns [Colombano (2019)], the detection area for the dielectric probes is estimated
168 at around 2 mm of the probe (Figure 2) [Colombano (2019)].

169



170

171 Figure 2: Position of dielectric probes in the 2D tank with associated detection areas for DNAPL

172
173
174
175
176
177
178
179
180
181
182
183
184
185
186
187
188
189
190
191
192
193
194
195
196
197

The permittivity values were corrected relative to the reference values measured in air and water using the following equation (Eq. 1) [Kargas and Soulis (2012)]:

$$\epsilon_{corrected} = \frac{\epsilon_{w-theoretical}(\epsilon_{meas} - \epsilon_{air})}{(\epsilon_w - \epsilon_{air})} + \epsilon_{air-theoretical} \quad \text{Eq. 1}$$

where $\epsilon_{w-theoretical}$ (-) is the relative permittivity of pure water ($\epsilon_{w-theoretical}=80$ at 20 °C), ϵ_{meas} (-) is the effective relative permittivity of the medium measured with the dielectric probe during the experiments, ϵ_{air} (-) is the relative permittivity of air measured at the beginning of the experiment, ϵ_w (-) is the relative permittivity of tap water measured at the beginning of the experiment, and $\epsilon_{air-theoretical}$ (-) is the theoretical relative permittivity of pure air ($\epsilon_{air-theoretical}=1$).

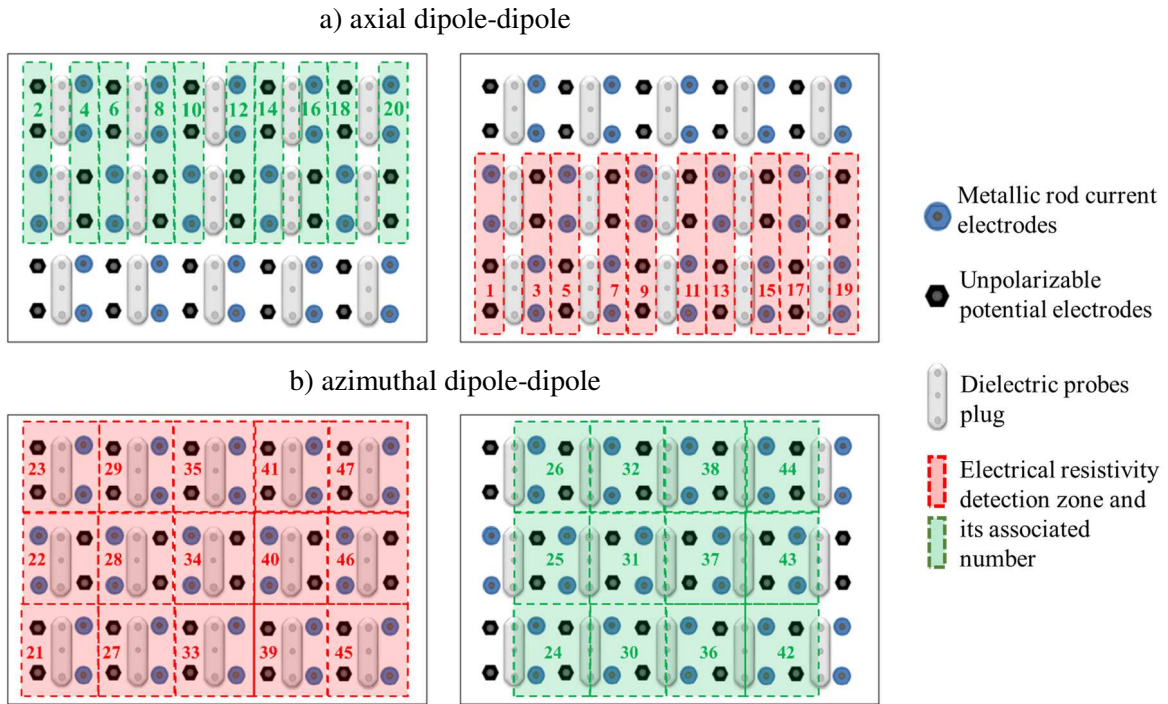
Permittivity measurements in these detection areas were compared with image interpretations (which allow to estimate the average water saturation in the same detection areas).

2.3 Electrical resistivity monitoring

Electrical resistivity was monitored using unpolarizable potential electrodes for voltage measurement, metallic stainless electrodes for current injection, a digital resistivity meter and a data acquisition software. Cu/CuSO₄ unpolarizable electrodes were used after preparation according to the method developed by Noel (2014) and derived from Mainault (2004) [Mainault et al. (2004); Noel (2014)]. The current injection electrodes were made of stainless Inox 316L. The resistivity meter was SIP LAB IV and we injected sinusoidal current shape. We recorded data using a frequency of 1.4 Hz because it is close to the one used in the field [Chambers et al. (2004); Constable and Srnka (2007); Han et al. (2015); Deparis et al. (2019)]. In total, 30 unpolarizable potential Cu/CuSO₄ electrodes and 30 metallic rod stainless current electrodes were arranged on the back of the 2D tank. On the basis of experiments conducted in 1D cells and 1D columns [Colombano (2019)], the detection areas for resistivity was estimated at approx. 2.50 mm around those electrodes (Figure 3) for porous media saturated with DNAPL. Two dipole-dipole injection and reception configurations were programmed (vertical and crossed).

198

199



200 Figure 3: Position of unpolarizable potential and current injection electrodes in the 2D tank with
 201 associated detection areas for DNAPL: a) axial dipole-dipole and b) azimuthal dipole-dipole
 202

203 In all, there were 47 resistivity monitoring zones. The electrode configurations were axial dipole-
 204 dipole (for the vertical line detection areas) and azimuthal dipole-dipole (for square detection areas).
 205 The values measured were resistance values, R_e , which were transformed into apparent electrical
 206 resistivity values, ρ_c , using the geometric coefficient, K_g (Eq. 2 and Eq. 3) [Reynolds (2011)]:

$$K_g = \frac{\rho_0}{R_e} \quad \text{Eq. 2}$$

$$\rho_c = R_e K_g \quad \text{Eq. 3}$$

207 where K_g (m) is the geometric coefficient, ρ_0 ($\Omega \cdot m$) is the measured resistivity value using a
 208 reference liquid, R_e (Ω) is the electrical resistance measured with SIP system using a reference liquid,
 209 and ρ_c ($\Omega \cdot m$) is the electrical resistivity of the bulk.

210 The conductivity of the tap water, measured at the beginning of each experiment, made it possible
 211 to determine ρ_0 and to calculate K_g (using Eq. 2) with filling 2D tank with water only. The value of K_g
 212 was then used throughout the experiment to transform R_e into ρ_c (using Eq. 3).

213

214 3. Theory

215 The relative permittivity, ε_r , is defined as the ratio of the real dielectric permittivity, ε' , and the free
 216 space permittivity, ε_0 (Eq. 4):

$$\varepsilon_r = \frac{\varepsilon'}{\varepsilon_0} \quad \text{Eq. 4}$$

217 where ε_r ($=\varepsilon$) (-) is the relative permittivity, ε' (F.m^{-1}) is the real dielectric permittivity, and ε_0
 218 (F.m^{-1}) is the free space permittivity.

219 In this article, later, all dielectric permittivity values are expressed relatively. In addition, for the
 220 sake of simplification, ε_r will be called ε .

221 The dielectric probe instrument sends a high-frequency electromagnetic step pulse through a
 222 transmission line of known length L , and the pulse is reflected back at the end of the line. From the
 223 travel time of the pulse analysis, the soil's bulk dielectric constant is computed [Topp et al. (1980);
 224 Persson and Berndtsson (2002)]. The dielectric constant can be calculated as (Eq. 5):

$$\varepsilon = \left(\frac{c_\varepsilon}{v_\varepsilon} \right)^2 \quad \text{Eq. 5}$$

225 where: c_ε (m.s^{-1}) is the speed of light (velocity of electromagnetic waves) in vacuum
 226 ($c_\varepsilon = 299\,792\,458 \text{ m.s}^{-1}$), v_ε (m.s^{-1}) is the function of the propagation velocity ($v_\varepsilon = 2L_\varepsilon/t_\varepsilon$), L_ε (m) is
 227 the waveguide length, and t_ε (s) is the travel time for the pulse to traverse the length of the
 228 embedded waveguide (down and back: $2L$).

229 The CRIM model for multi-phase dielectric permittivity is based on Eq. 6 [Birchak et al. (1974);
 230 Roth et al. (1990); Endres and Knight (1992)]:

$$\varepsilon = \left[\sum_{i=1}^N v_i \varepsilon_i^{\alpha_\varepsilon} \right]^{1/\alpha_\varepsilon} \quad \text{Eq. 6}$$

231 where ε (-) is the effective relative permittivity of the multi-phase system, ε_i (-) is the relative
 232 permittivity of the i phase, v_i (-) is the volume fraction of the i phase, and α_ε (-) is an empirical
 233 constant related to the geometry of the grains and their spatial distribution.

234 Ajo-Franklin *et al.* (2004) report that for a three-phase mineral/water/NAPL (TCE) mixture and
 235 assuming that $\alpha_\varepsilon=0.5$, the CRIM equation becomes (Eq. 7) [Ajo-Franklin et al. (2004)]:

$$\varepsilon = [\emptyset(S_w\sqrt{\varepsilon_w} + S_n\sqrt{\varepsilon_n}) + (1 - \emptyset)\sqrt{\varepsilon_s}]^2 \quad \text{Eq. 7}$$

236 where \emptyset (-) is the porosity, S_w (-) is the water (wetting fluid) saturation, ε_w (-) is the relative
 237 permittivity of water, S_n (-) is the DNAPL (non-wetting fluid) saturation, ε_n (-) is the relative
 238 permittivity of DNAPL, and ε_s (-) is the relative permittivity of soil particles.

239 The values measured were resistance values, R_e , which were transformed into apparent electrical
 240 resistivity values, ρ_c , using the geometric coefficient, K_g , (Eq. 2 and Eq. 3), as explained in the section
 241 2.3.

242 Archie's law (1942), adapted by Winsauer et al. (1952), describes how resistivity depends on
 243 porosity if ionic conduction in the pore fluid dominates other conduction mechanisms in the rocks (Eq.
 244 8) [Archie (1942); Winsauer et al. (1952)]:

$$\emptyset\rho_c = \rho_{c,w}a_c\emptyset^{-m_c} \quad \text{Eq. 8}$$

245 where ρ_c ($\Omega.m$) is the electrical resistivity of the bulk, $\rho_{c,w}$ ($\Omega.m$) is the electrical resistivity of the
 246 water at temperature T, a_c (-) is an empirical parameter (typically equal to 1 but that can vary from <1
 247 for intergranular porosity to > 1 for joint porosity), and m_c (-) is the cementing factor (also an
 248 empirical parameter usually approximately equal to 2, but that can vary from 1.2 for unconsolidated
 249 sediments to 3.5 for crystalline rocks; Friedman (2005) produced an exhaustive list of cementation
 250 exponent value [Friedman (2005)]).

251 Adapted Archie's law (referred to as Archie's law in the rest of the document) seems to be a good
 252 approximation when the conductivity is controlled by electrolytic conduction, which is often the case
 253 for non-consolidated porous media with a low clay content [Árnason et al. (2000)]. Glover (2010) has
 254 proposed, on the basis of Archie's law, the following equations for calculating S_w for a two-phase system,

255 where the conductivity of GB is neglected as it is very low ($\sigma_{c,GB}=10^{-20}$ S.m⁻¹) (Eq. 9 to Eq. 12) [Glover
256 (2010)]:

$$\sigma_{c,bulk} = \sigma_{c,DNAPL}[\phi(1 - S_w)]^{m_1} + \sigma_{c,water}[\phi(S_w)]^{m_2} \quad \text{Eq. 9}$$

$$\left(-\frac{\phi_1^2}{2}\right)m_2^2 + \left(\phi_1 + \frac{\phi_1^2}{2}\right)m_2 - \phi_1^{m_1} = 0 \quad \text{Eq. 10}$$

$$m_2 = \frac{-\left(\phi_1 + \frac{\phi_1^2}{2}\right) \pm \left[\left(\phi_1 + \frac{\phi_1^2}{2}\right)^2 - 4\left(-\frac{\phi_1^2}{2}\right)(-\phi_1^{m_1})\right]^{\frac{1}{2}}}{-\phi_1^2} \quad \text{Eq. 11}$$

$$m_2 = \frac{-(4\phi_1 + 2\phi_1^2) \pm (4\phi_1^2 + 4\phi_1^3 + \phi_1^4 - 8\phi_1^2\phi_1^{m_1})^{\frac{1}{2}}}{-4\phi_1^2} \quad \text{Eq. 12}$$

257 where $\sigma_{c,bulk} = \sigma_c$ (S.m⁻¹) is the electrical conductivity of the bulk, $\sigma_{c,DNAPL}$ (S.m⁻¹) is the
258 electrical conductivity of DNAPL, m_1 (-) is the cementation exponent of DNAPL phase, $\sigma_{c,water}$
259 (S.m⁻¹) is the electrical conductivity of water, m_2 (-) is the cementation exponent of water phase, and
260 $\phi_1 = \phi(1 - S_w)$; $\phi_2 = \phi(S_w)$.

261 The DNAPL-water interface charges (*i.e.* surface conductivity) have been neglected because i. the
262 specific surface is negligible (surface tension is high) [Brusseu et al. (2006); Linde et al. (2007)] and,
263 ii. the ionic exchanges between the two phases are weak (DNAPL is poorly soluble in water) [Revil
264 (2017)].

265

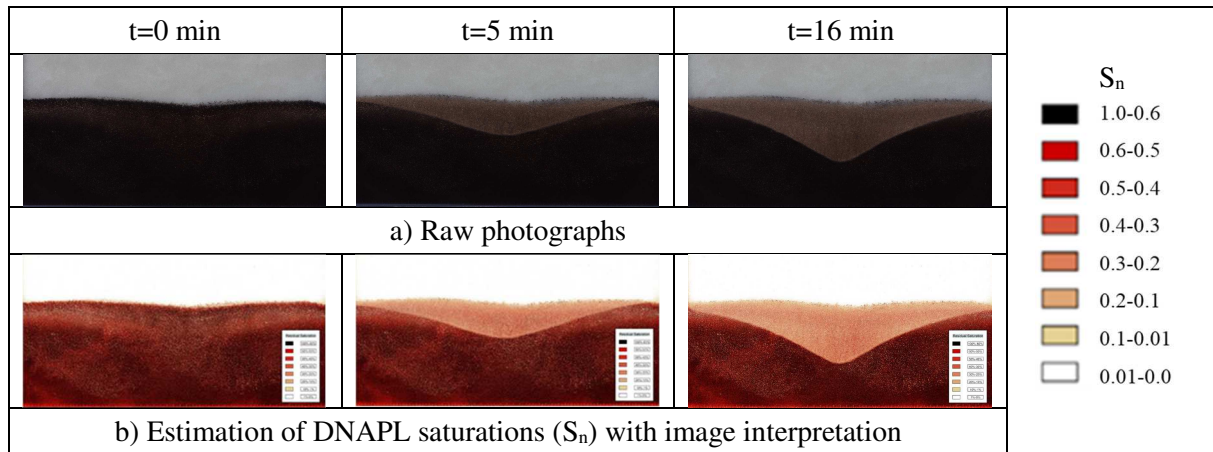
266 4. Results and discussion

267 Previous work has shown that one can accurately determine water and DNAPL saturations by
268 image interpretation during drainage-imbibition experiments in 1D cells and pumping experiments in
269 2D tank [Colombano (2019); Colombano et al. (2020); Irvani et al. (2020b); Philippe et al. (2020);
270 Colombano et al. (2021)]. The purpose of the experiments presented here is to compare the measured
271 permittivities and electrical resistivities with those estimated on the basis of the water saturations
272 determined using image interpretation. Figure 4 shows raw photographs and estimations of DNAPL
273 saturations with image interpretation during a pumping experiment conducted with 0.5 mm GB with a

274 flow rate of

275 150 mL.min⁻¹ and without enhancement.

276

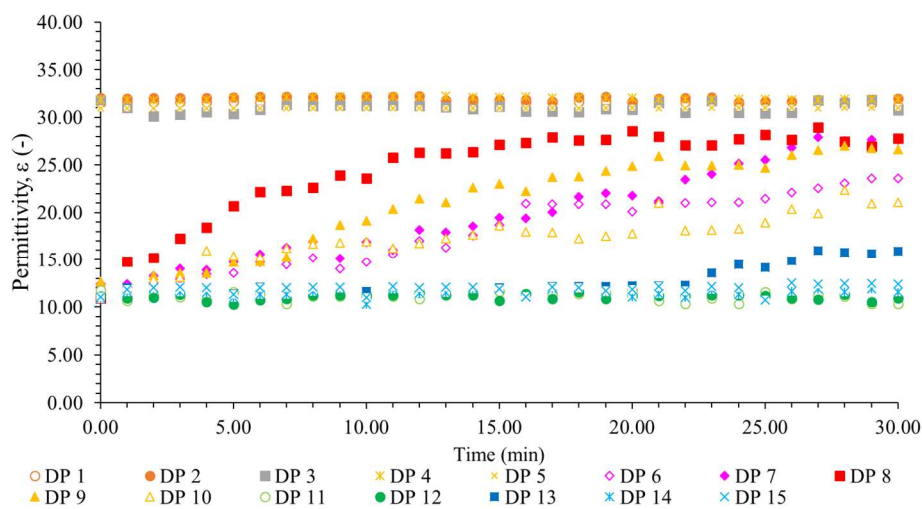


277 Figure 4: Illustration of a pumping experiment with 0.5 mm GB with a flow rate of 150 mL.min⁻¹
 278 (without enhancement): a) raw photographs and b) estimation of DNAPL saturations (S_n) with image
 279 interpretation
 280

281 4.1 Permittivity monitoring

282 4.1.1 Experiments without enhancement

283 Figure 5 shows changes in permittivity, ϵ (corrected relative to the reference value of air and water
 284 measured at the beginning of the experiment, see Eq. 1) as a function of time during a pumping experiment
 285 conducted with 0.5 mm GB with a flow rate of 150 mL.min⁻¹ and without enhancement (the locations of
 286 the dielectric probes (DP) are shown in Figure 2).
 287



288
 289 Figure 5: Evolution of the permittivity in the 2D tank with 0.5 mm GB with a flow rate of
 290 150 mL.min⁻¹ (without enhancement)

291

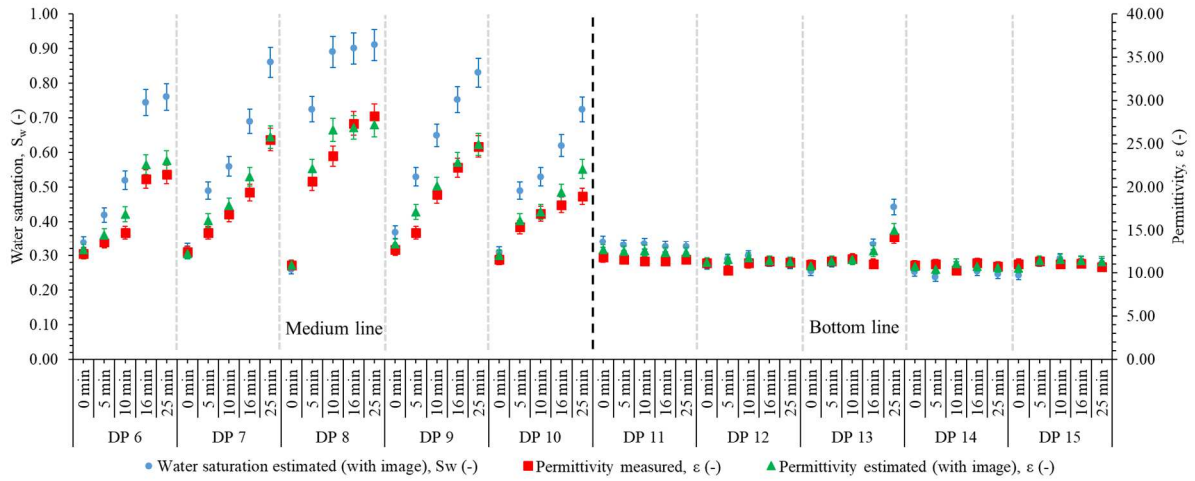
292 DP 1 to 5 located in the upper part of the 2D tank (Figure 2) were only surrounded by water
293 ($S_w=1$). They had the same values when the experiments began (31.49 ± 0.51). These values were
294 similar to the ones measured and corrected by Colombano *et al.* (2020) in the 1D cells.

295 DP 11 to 15 were in the lower portion of the 2D tank (Figure 2). As pumping began, the water
296 contents were equivalent to S_{rw} . The monitored permittivities for S_{rw} were around 11.39 ± 0.39 and
297 agreed with those measured and corrected by Colombano *et al.*, 2020 in the 1D cells and columns. As
298 pumping ended, DP 13, located in the lower central position, detected the arrival of the cone of
299 depression (at $t=23$ min). DP 6 to 10 were in the middle of the 2D tank (Figure 2). Logically DP 8,
300 located in the tank's centre, was the first to measure the permittivity increase; then as pumping
301 continued, DP 7 and 9, located on either side of this central position, showed increased permittivities
302 (and therefore decreasing DNAPL saturations). As pumping ended, ϵ_{meas} at DP 7 to 9 were on average
303 27.27 ± 1.10 , which matches with measurements at the end of imbibition in 1D cells and 1D columns
304 [Colombano *et al.* (2020)]. The ϵ_{meas} at DP 6 and 10 (located at the cone of depression) were
305 respectively
306 23.41 ± 0.29 and 21.46 ± 0.77 .

307 Figure 6 shows variations in water saturation, measured permittivity and estimated permittivity
308 during the pumping experiment. The water saturation was calculated from image interpretation (*i.e.*
309 from optical densities in the DP's detection area). The permittivity estimate was calculated from S_w
310 and
311 Eq. 13 for 0.5 mm GB (adaptation of the CRIM model from drainage-imbibition experiments
312 [Colombano *et al.* (2020)]).

$$\epsilon = [\emptyset(S_w \epsilon_w^{0.7} + S_n \epsilon_n^{0.7}) + (1 - \emptyset) \epsilon_s^{0.7}]^{\frac{1}{0.7}} \quad \text{Eq. 13}$$

313



314

315 Figure 6: Average water saturation, measured and estimated permittivity during the pumping
 316 experiment in the 2D tank with 0.5 mm GB and a flow rate of 150 mL.min⁻¹ (without enhancement)
 317

318

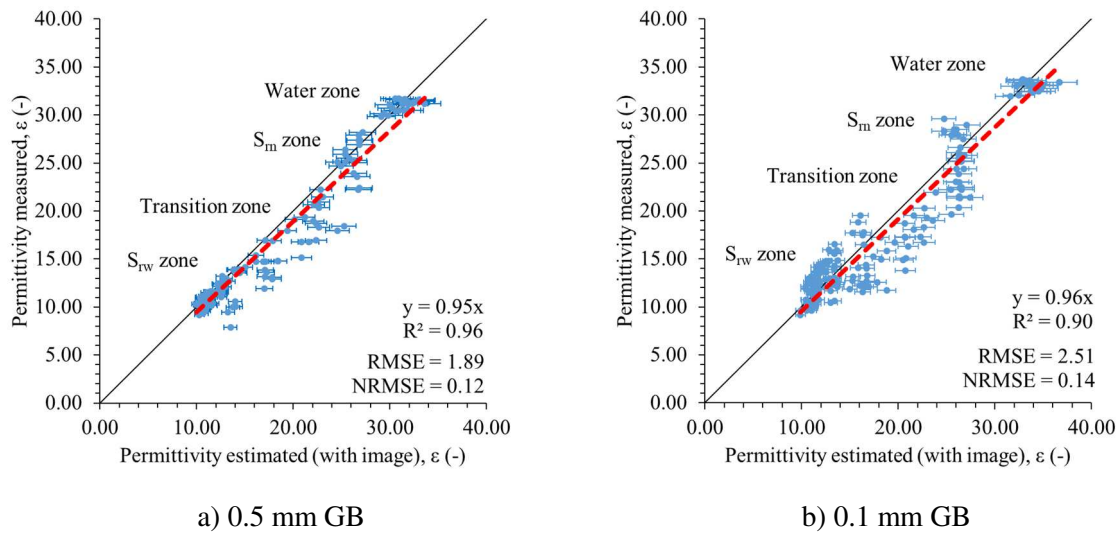
319 The ϵ_{est} (from image interpretations) were very similar to the ϵ_{meas} at the start and end of pumping.
 320 When the migration front moved to the DP's detection area, the ϵ_{meas} were systematically lower than
 321 the ϵ_{est} . The value assigned to S_w is the average of the S_w at the detection area. This value is
 322 transformed into permittivity according to the CRIM model. This model is only valid for
 323 homogeneous media. When the detection area is crossed by the migration front, this zone is a mixing
 324 of contents similar to the residual saturation of DNAPL (S_{rn}) and contents similar to the residual
 325 saturation of water (S_{rw}). Therefore, for two heterogeneous zones, the weight of the portion
 326 characteristic of S_{rw} influences the global ϵ_{meas} more than the portion characteristic of S_{rn} . Eq. 6,
 327 combined with the permittivity values for DNAPL and water ($\epsilon_n=3.11$ and $\epsilon_w=80$), shows that the
 328 propagation velocity function is 6 times faster for DNAPL than for water. It is therefore consistent
 329 that, when the DP detection area is crossed by the migration front, ϵ_{meas} is systematically lower than
 330 ϵ_{est} .

331 This shift between the estimated and measured permittivities in the transition zones was studied for
 332 soils in the unsaturated zone (soil-air-water system). Some authors have shown that the CRIM model
 333 (based on the permittivity of free water, of air and solids) may not be suitable in all situations,
 334 especially in the transition phases (when S_w are between S_{rn} and S_{rw}). These authors have proposed to
 consider a 4th constituent, the bound water (whose dielectric constant is very different from that of free

335 water) [Dasberg and Hopmans (1992); Capparelli et al. (2018)]. An equation derived from the CRIM
 336 model incorporating the bound water has been proposed [Dobson et al. (1985); Dirksen and Dasberg
 337 (1993)]. Capparelli et al. (2018) carried out monitoring of S_w variations with dielectric probes in
 338 unsaturated soils. The experimental results were compared to the classical CRIM model, but also to
 339 the four-phase dielectric mixing model (with bound water), and the classical CRIM model with a
 340 variable exponent. The best results were obtained with the three-phase dielectric mixing model with a
 341 variable exponent (α_ϵ) [Capparelli et al. (2018)].

342 Figure 7 compares measured and estimated permittivity (with image interpretation) in the 2D tank
 343 for 0.5 and 0.1 mm GB packings in the absence of any enhancement.

344



345 Figure 7: Comparison of measured and estimated permittivity (with image interpretation) in the 2D
 346 tank with a flow rate of $150 \text{ mL} \cdot \text{min}^{-1}$ (without enhancement) for a) 0.5 and b) 0.1 mm GB

347

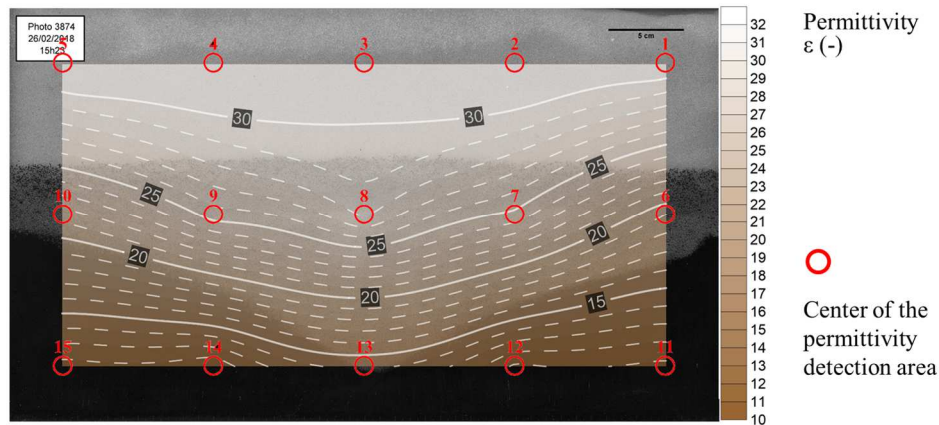
348 Normalized root-mean-square error (NRMSE) were 0.12 and 0.14 for 0.5 and 0.1 mm GB,
 349 respectively. The measured permittivities agreed with the estimated permittivities (based on image
 350 interpretation). As expected, NRMSE for the 0.5 mm GB was lower than for the 0.1 mm GB, which
 351 shows superior correlation in the case of 0.5 mm GB (because of the fingering process which is more
 352 pronounced for 0.1 mm GB). In both cases, four distinct zones appear:

- 353 • A S_{rw} zone with ϵ values around 10.50 to 12.00 for the 0.5 mm GB and 12.50 to 13.50 for the
 354 0.1 mm GB (start of pumping)

- A transition zone with values between the S_{rw} zone and the S_{rn} zone; here the majority of points were below the linear regression line (ϵ_{meas} are below ϵ_{est}),
- A S_{rn} zone with values around 27.00 to 28.00 for the 0.5 mm GB and 25.00 to 26.00 for the 0.1 mm GB (end of pumping),
- A water zone which corresponds to ϵ_{meas} at DP 1 to 5 (where $S_w=1$), with 31.00 to 32.00 for 0.5 mm GB and 32.00 to 33.00 for 0.1 mm GB.

Figure 8 displays a surface plot of the permittivity measured on an image at the end of pumping experiment. The permittivity values were calculated using an interpolation technique (Kriging or Gaussian process regression) with Surfer® software.

364



365

Figure 8: Surface plot of measured permittivity within an image with 0.5 mm GB and a flow rate of 150 mL.min⁻¹ (without enhancement) at t=18 min

368

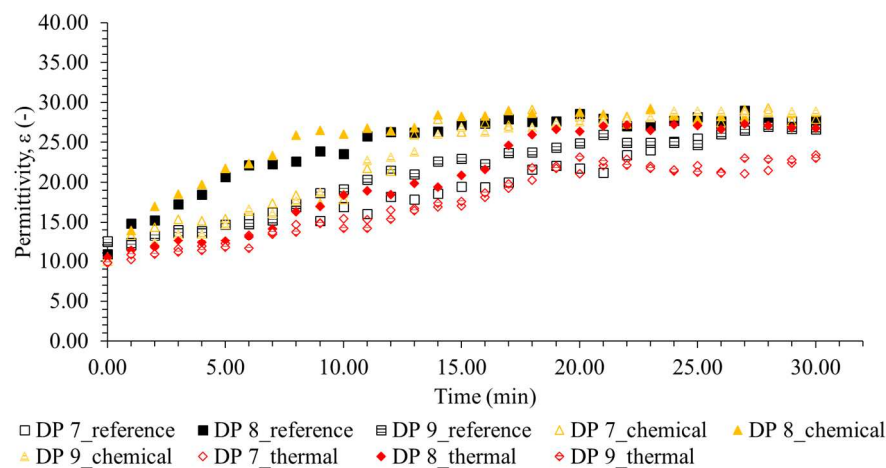
One can see that the permittivity and the S_n do not overlap completely. This is explained by two phenomena: i. the kriging method (under Surfer® software) is only based on 15 points; ii. the transition zones cause an offset for the measurements. However, this does illustrate that the cone of depression can be determined by permittivity monitoring.

373

374 4.1.2 Experiments with chemical or thermal enhancement

375 The modelling and experimental results show that chemical enhancement has a beneficial effect on
 376 recovered DNAPL volumes. The use of chemical enhancement was proportionally more advantageous
 377 for lower flow rates than for higher ones. The cone of depression radius and height increased with
 378 added surfactant. Thermal enhancement had no beneficial effect on DNAPL recovery rate or yield.
 379 Heating the porous media had a negative effect on cone of depression radius and height [Colombano
 380 et al. (2021)]. Figure 9 shows a comparison of measured permittivity in the 2D tank (with and without
 381 enhancements) for 0.5 mm GB. Figure 9 also shows that by using DP it is possible to assess the
 382 differences in remediation yields and rates between recovery of free product without enhancement,
 383 with chemical enhancement and with thermal enhancement. The DP located at the heart of the cone of
 384 depression globally showed faster and larger variations in permittivities for chemical enhancement
 385 than without enhancement (this is more visible for the 0.1 GB than for the 0.5 mm GB). Compared to
 386 the reference (no enhancement), the DP monitoring data show that with chemical enhancement, the
 387 radius of action of the cone of depression is higher, the S_n are lower and the S_n fall faster than without
 388 enhancement. Moreover, the low NRMSE values, *i.e.* around 0.10 for 0.5 mm GB and lower than 0.14
 389 for 0.1 mm GB (calculated based on graphs $\epsilon_{meas}=f(\epsilon_{est})$), suggest that the S_n can be quantified from the
 390 dielectric probes (see Figure 1A and Figure 2A, Appendix).

391



392

393 Figure 9: Evolution of measured permittivity in the 2D tank for 0.5 mm GB with a flow rate of

394

150 mL.min⁻¹ (with and without enhancements)

395

396 S_n can be quantified accurately from the dielectric probes with and without enhancement, except
397 for the transition zone. It is possible to highlight the differences in remediation yield and rate with
398 permittivity measurements, but the detection area is spatially limited.

399

400 4.2 *Electrical resistivity monitoring*

401 4.2.1 *Experiments without enhancement*

402 Figure 10 shows changes in resistivity as a function of time during the pumping experiment
403 conducted with 0.5 mm GB with a flow rate of 150 mL.min⁻¹ (without enhancement). The resistivity
404 values were calculated from Eq. 2 and conductivity measurements obtained from blank test (reference)
405 before starting the experiments.

406

417 (ρ_c) decreased for R10, located in the central section of the cone of depression. Logically the other
 418 detection areas located in more lateral positions of the cone of depression had smaller and delayed
 419 reductions. We saw the same phenomena for the vertical line detection areas in the lower section (odd
 420 numbers between R1 and R9). ρ_c value is divided by a factor of 4 in the first 5 minutes for R9 (which
 421 is in the central part of the 2D tank).

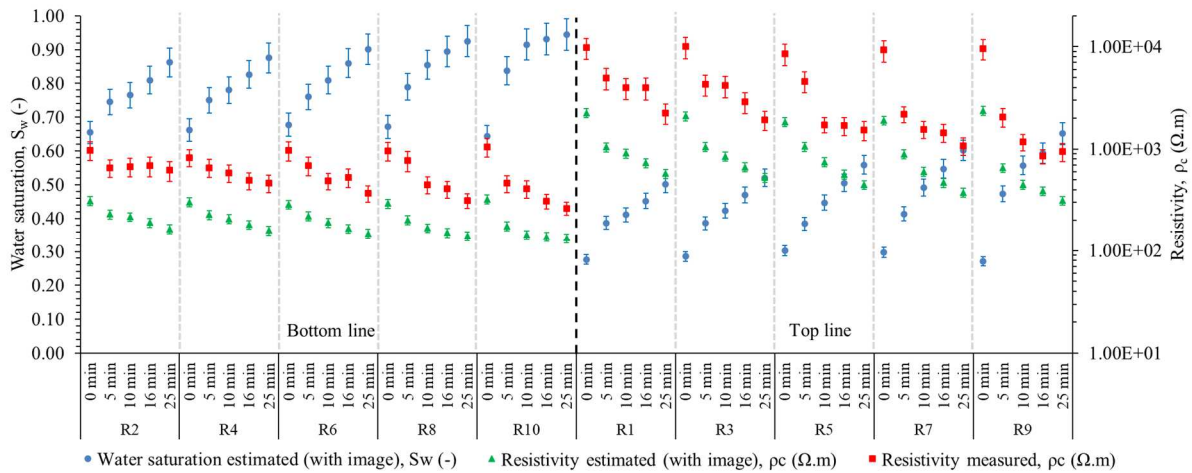
422 The square detection areas were arranged along three horizontal lines: the top line only in contact
 423 with water (in blue in Figure 10 b), the medium line at the upper portion of the DNAPL (in yellow),
 424 the bottom line at the lower portion of the DNAPL (in red). The resistivities measured in the top line
 425 and in the bottom line were relatively constant during the experiment. The resistivities measured at
 426 R33 (located in the center of the bottom line) decreased slightly, which shows that the cone of
 427 depression partially reached this area. As for the medium line, the resistivities at R34 (located at the
 428 center of the 2D tank) decreased faster. At the end of pumping, this area was completely filled by
 429 values around S_m (according to the image interpretations).

430 Figure 11 shows how water saturation, measured and estimated resistivity varied during the
 431 pumping experiment. Transforming optical density into S_w allows a mean S_w value to be assigned by
 432 detection area. This value is transformed into resistivity according to Eq. 14 for 0.5 mm GB
 433 (adaptation of the Archie's law from drainage-imbibition experiments [Colombano et al. (2020)]).

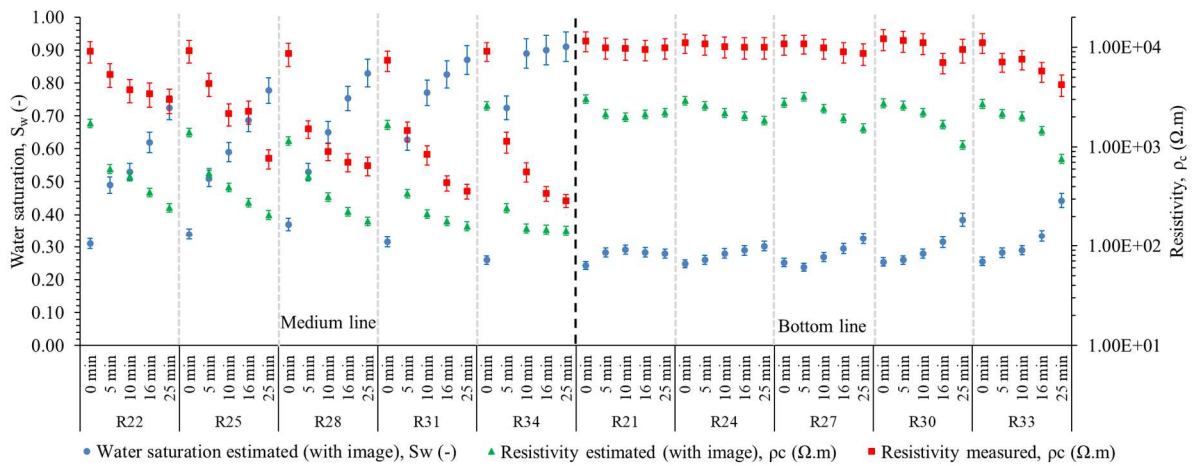
$$\rho_c = \frac{1}{\sigma_{c,bulk}} = \frac{1}{\sigma_{c,DNAPL}[\phi(1 - S_w)]^{1.752} + \sigma_{c,water}[\phi(S_w)]^{1.9}} \quad \text{Eq. 14}$$

434

435



a) R1 to R10: vertical line detection areas (axial dipole-dipole)



b) R21 to R34: square detection areas (azimuthal dipole-dipole)

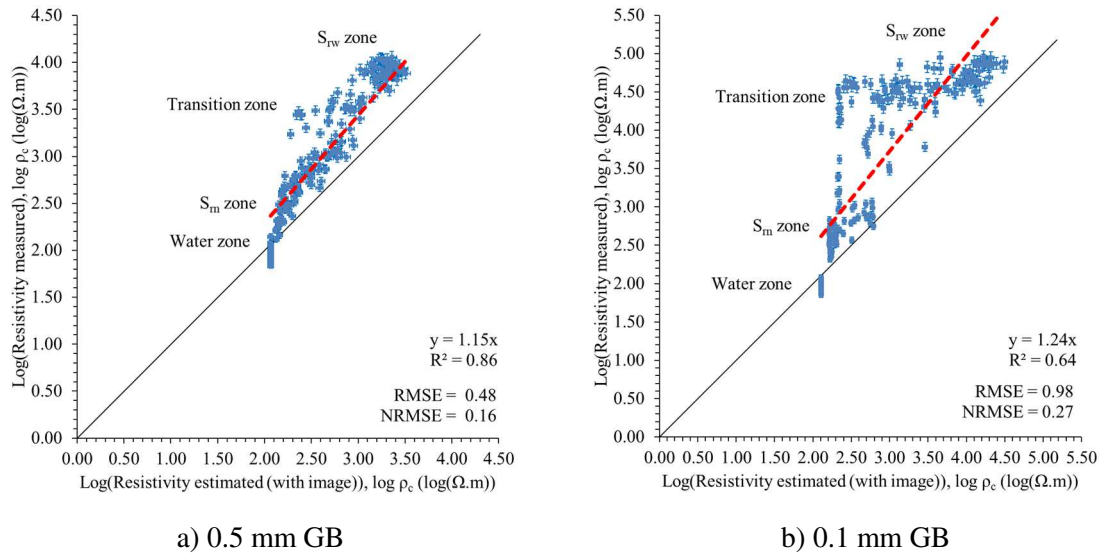
437 Figure 11: Average water saturation, measured and estimated resistivity during the pumping
 438 experiment in the left and central parts of the 2D tank with 0.5 mm GB with a flow rate of
 439 150 mL.min⁻¹ (without enhancement) – a) R1 to R10 and b) R21 to R34
 440

441 Globally, one see that the variations in $\rho_{c,meas}$ match the variations in $\rho_{c,est}$. However, these
 442 variations show that the differences between the $\rho_{c,meas}$ and $\rho_{c,est}$ are not constant. The fitting for the
 443 experiments with Archie’s law (during the experiments in 1D cells and 1D columns) was not as good
 444 as for the permittivities [Colombano et al. (2020)]. The $\rho_{c,meas}/\rho_{c,est}$ ratios increase as the resistivity
 445 values increase. The differences between the estimated and measured resistivities may have several
 446 causes:

- 447 • In a porous medium filled with non-wetting and wetting fluids, considering a suitable
448 cementation factor that considers the saturation condition, a better estimation of resistivity
449 with Archie's law would be possible [Byun et al. (2019)].
- 450 • At a pore scale, the resistivity indexes did not generally obey Archie's law in the non-
451 homogeneous zones (for example with a transition zone constituted of values close to S_m and
452 S_{rw}). The water films play a role not only on the pore space connectivity but also on resistivity;
453 therefore, we can over or underestimate resistivity depending on the thickness of these water
454 films around grains of sand or glass beads [Bernabé et al. (2011); Li et al. (2015); Bernabé
455 et al. (2016)].
- 456 • Many other parameters could be considered at different scales in electrical conductivity
457 models in porous media: tortuosity, pore size distribution, pore-conductance distributions,
458 interconnectivity and universal power law of percolation [Glover (2010); Cai et al. (2017);
459 Ghanbarian and Sahimi (2017)]. Jougnot et al. (2018) reported that the distribution between
460 wetting and non-wetting fluids (with different electrical conductivity) in porous media and the
461 resulting heterogeneity lead to electrical current channelling with strong effects on bulk
462 conductivities. They suggest a strong impact of pore-scale on upscaled bulk electrical
463 conductivity in terms of magnitude and anisotropy [Jougnot et al. (2018)].

464 These parameters have not been considered in our experiments. However, Figure 12 shows that it is
465 possible, as a first approach, to establish correlations between $\rho_{c,meas}$ and $\rho_{c,est}$. Figure 12 compares the
466 measured and estimated resistivity (with image interpretation) in the 2D tank for 0.5 and 0.1 mm GB.

467



468 Figure 12: Comparison of measured and estimated resistivity (with image interpretation) in the 2D
 469 tank with a flow rate of $150 \text{ mL} \cdot \text{min}^{-1}$ (without enhancement) for a) 0.5 and b) 0.1 mm GB

470

471 The NRMSE were 0.16 and 0.27 for 0.5 and 0.1 mm GB, respectively. The NRMSE values are
 472 quite high, which shows that the measured permittivities were not well correlated with the estimated
 473 permittivities (based on image interpretation). Moreover, the NRMSE was lower for the 0.5 mm GB
 474 than for the 0.1 mm GB because of the fingering process which is more pronounced for 0.1 mm GB.
 475 The data dispersivities were quite high, in particular for the 0.1 mm GB for which the fingerings and
 476 heterogeneities in DNAPL distribution were clearly visible.

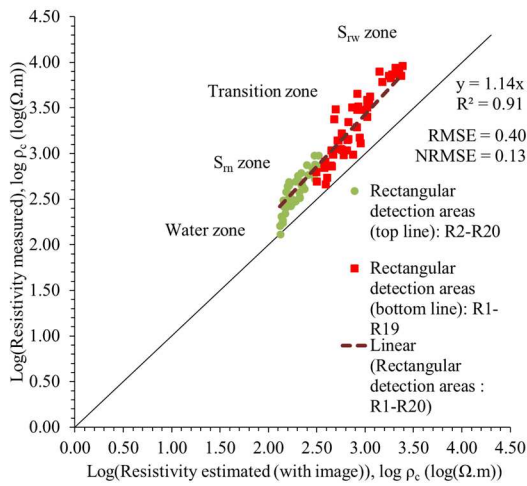
477 For values corresponding to zones close to the S_{rw} (*i.e.* when all of the detection area had values
 478 close to the S_{rw}), the $\rho_{c,meas}/\rho_{c,est}$ ratios were close to those determined during the 1D cell and 1D
 479 column experiments [Colombano et al. (2020)]; these ratios were on average 2.97 for 0.5 mm GB and
 480 4.32 for 0.1 mm GB. In large part, these ratios explain the slopes of above one ($y = 1.15x$ and $y =$
 481 $1.24x$ for
 482 0.5 mm GB and 0.1 mm GB, respectively).

483 For values close to the S_m (when all of the detection area has values close to the S_m), the $\rho_{c,meas}/\rho_{c,est}$
 484 ratios were close to those determined during the 1D cell and 1D column experiments; these ratios were
 485 on average 1.05 for 0.5 mm GB et 2.3 and 0.1 mm GB (taking into account the correction factors).

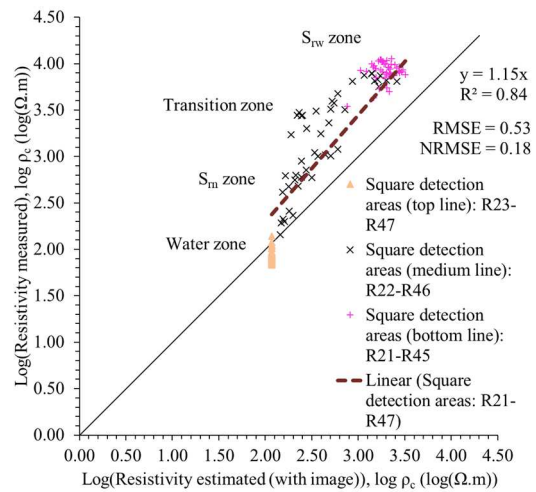
486 A transition zone was visible between the two previously mentioned zones. These were the
487 detection areas for the DNAPL-water interface (and therefore, the values close to both S_{rw} and S_m). In
488 this zone, the $\rho_{c,meas}/\rho_{c,est}$ ratio was variable but globally higher than those determined for the zone
489 relative to S_m . These ratios are the second explanation for the slopes of the curves. Therefore, we can
490 distinguish, just like for permittivity, four distinct zones (Figure 13):

- 491 • S_{rw} zone: start of pumping
- 492 • Transition zone: this zone corresponds to values between the S_{rw} zone and the S_m zone; here,
493 the majority of points were above the linear regression line ($\rho_{c,meas}$ are above $\rho_{c,est}$),
- 494 • S_m zone: end of pumping,
- 495 • Water zone: this zone corresponds to the detection areas situated in the upper zone of the 2D
496 tank.

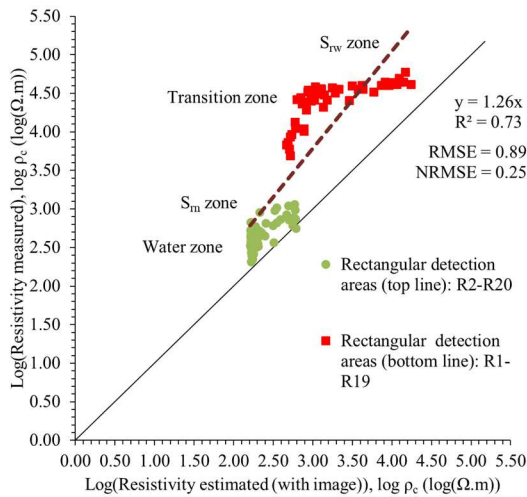
497



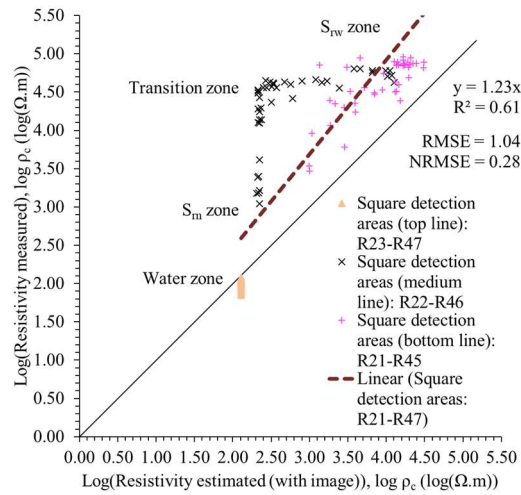
a) 0.5 mm GB-vertical line detection areas
(axial dipole-dipole)



b) 0.5 mm GB-square detection areas
(azimuthal dipole-dipole)



c) 0.1 mm GB-vertical line detection areas
(axial dipole-dipole)



d) 0.1 mm GB-square detection areas
(azimuthal dipole-dipole)

499 Figure 13: Comparison of measured and estimated resistivity (with image interpretation) in the 2D
 500 tank with a flow rate of 150 mL.min⁻¹ (without enhancement) for a) 0.5 mm GB-vertical line detection
 501 areas, b) 0.5 mm GB-square detection areas, c) 0.1 mm GB-vertical line detection areas,
 502 d) 0.1 mm GB-square detection areas

503
 504 The vertical line detection areas (axial dipole-dipole electrode configurations) all correspond to the
 505 transition zone. The areas of the bottom line (red dots) are the furthest from the linear regression. The

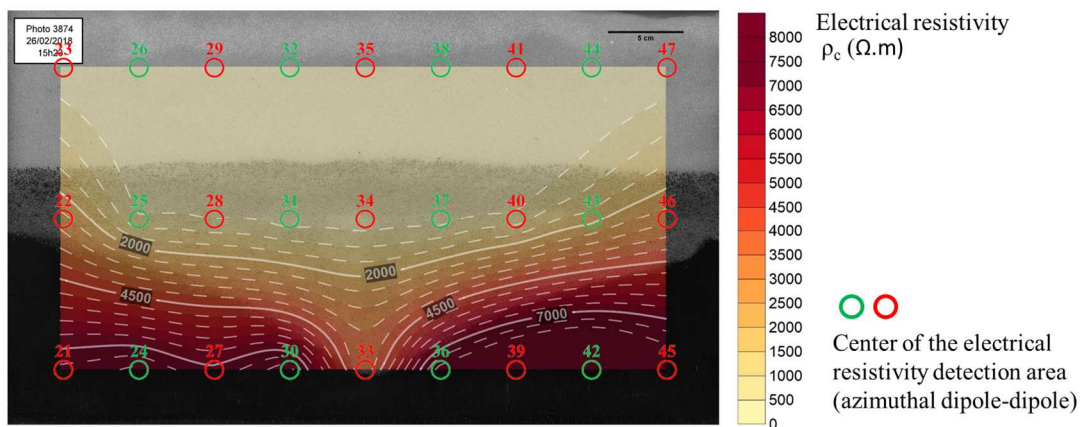
506 areas of the top line (green dots), filled largely by water, are obviously closer to the linear regression
507 line (the calibrations are better for low resistivities).

508 As for the square detection areas (azimuthal dipole-dipole electrode configurations), the top line
509 measurements (brown dots), corresponding to $S_w=1$, agree with the estimation perfectly. The bottom-
510 line measurements (pink dots) corresponding to S_{rw} , are overestimated by the factors previously
511 described. The points outside the group of dots correspond to the arrival of the cone of depression. In
512 that case, the dots get further from the linear regression line (this is the transition zone). Finally, the
513 measurements at the medium line (black dots) correspond in large part to the transition zone and are
514 further from the linear regression line.

515 For lower resistivity values (corresponding to the detection areas entirely concerned with S_m) and
516 for the highest resistivity values (corresponding to zones entirely concerned with S_{rw}), we see that the
517 points of course fall closer to the linear regression line.

518 Figure 14 shows a surface plot of the resistivity measured on an image at the end of pumping
519 experiment.

520



521

522 Figure 14: Surface plot of measured resistivity with an image with 0.5 mm GB and a flow rate of

523

150 mL.min⁻¹ (without enhancement) at t=18 min

524

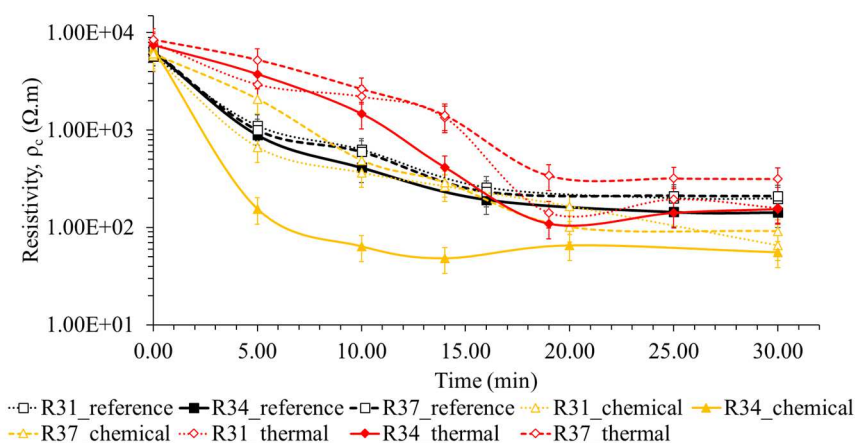
525 This image was made using Surfer® software with kriging method only with the square detection
 526 areas (R21 to R47). We see that although they are not perfectly superimposed, the resistivity
 527 measurements do show the cone of depression.

528

529 *4.2.2 Experiments with chemical or thermal enhancement*

530 Figure 15 shows a comparison of measured resistivity in the 2D tank (with and without thermal and
 531 chemical enhancements) for 0.5 mm GB with a flow rate of 150 mL.min⁻¹. The electrical resistivity
 532 monitoring had higher standard deviations (often in the order of 30%) than permittivity monitoring.
 533 Therefore, we cannot closely estimate the residual saturations from electrical resistivity alone.
 534 However, the precision was sufficient (especially, for values close to the S_m) to show differences
 535 between the three treatment technologies. Figure 15 shows that chemical enhancement has higher
 536 remediation yields and rates: the radius of action being higher, the S_n being lower and S_n falling more
 537 quickly. In contrast, the thermal enhancement was less effective with resistivity drops being lower and
 538 slower.

539



540

541 Figure 15: Evolution of the measured resistivity in the 2D tank for 0.5 mm GB with a flow rate of
 542 150 mL.min⁻¹ (with and without enhancements)

543

544 Figures 3A and 4A (Appendix) compare the measured and estimated resistivity (with image
 545 interpretation) in the 2D tank for 0.5 and 0.1 mm GB with chemical and thermal enhancements,

546 respectively. The results are consistent with those obtained without enhancement: we distinguish the
547 same 4 areas and the NRMSE are close to those obtained previously.

548 By combining electrical resistivity monitoring (which gives an integrative view of the cone of
549 depression) with DP (which gives precise but spatially limited data), and image analysing one can
550 better closely calibrate resistivities with S_w and better quantify remediation rates and yields.

551 As for applications at field conditions, the main methods for indirectly interpolating data between
552 boreholes (with soil analysis) are: piezometers (with water analysis) and soil-gas wells (with gas
553 analysis). Remediation monitoring by geophysical methods (including resistivities for DNAPLs) are
554 complementary and useful to better interpolate data between boreholes. The main monitoring
555 approach is based on differences in resistivities before, during and after treatment. However,
556 quantifying the S_n remains difficult. Monitoring the permittivities, continuously in the field, would
557 contribute to better quantify the S_n locally and to calibrate resistivity measurements on these points.
558 This permittivity/resistivity coupling would: i. better quantify S_n (during the diagnostic and
559 remediation phases); ii. limit field investigations by direct measurements (boreholes, soil-gas wells
560 and piezometers); and iii. improve remediation operations (by optimizing pumping flow rates and radii
561 of cone of depression as a function of the flows and pressures applied).

562

563 **5. Conclusions**

564 The objective of the DNAPL pumping experiments in the 2D tank was to validate permittivity and
565 electrical resistivity measurements and estimations using image interpretation. To achieve this, the
566 average optical densities (corresponding to the detection area for the dielectric probes) were
567 determined throughout the experiments. These optical densities were converted into water saturation
568 then into permittivities using the CRIM model (whose parameters were validated during previous 1D
569 cell and 1D column experiments). Comparison of ϵ_{meas} and ϵ_{est} between experiments without
570 enhancement, with chemical enhancement and with thermal enhancement shows very good
571 correlations. For instance, the NRMSE were 0.12 and 0.14 for 0.5 and 0.1 mm GB, respectively. This
572 shows that the measured permittivities agreed well with the image interpretation. As expected, the
573 NRMSE for the 0.5 mm GB was higher than for the 0.1 mm GB which indicates a better correlation of

574 values for 0.5 mm GB experiments, which display less fingering. All experiments clearly displayed
575 four distinct zones: S_{rw} zone (start of pumping), S_m zone (end of pumping), water zone (corresponding
576 to $S_w=1$), and transition zone (this zone corresponds to values between the S_{rw} and S_m zones). The
577 correlations are very good for the first three zones. For the transition zone, we see that the majority of
578 ε_{meas} were lower than ε_{est} . This is because when the detection area is crossed by the migration front,
579 this area displays both S_m and S_{rw} areas. Therefore, for two heterogeneous zones, the weight of the
580 portion similar to S_{rw} impacts on the global ε_{meas} more than the portion similar to S_m . This confirms
581 that the CRIM model is only valid for homogeneous media. It will be necessary to quantify this
582 transition zone using mixing models.

583 The image interpretation results were compared with measured resistivities. The average optical
584 densities (corresponding to the detection area of the dipole-dipole injection and reception
585 configurations) were determined throughout the experiments. These optical densities were transformed
586 by water saturation into resistivity using Archie's law. The comparison of results on $\rho_{c,meas}$ and $\rho_{c,est}$
587 were not very promising for any of the experiments, with or without enhancements. The NRMSE
588 varied between 0.16 and 0.27 for 0.5 and 0.1 mm GB, respectively. The $\rho_{c,meas}/\rho_{c,est}$ ratios were higher
589 for low S_w (close to the S_{rw}). Note that for low resistivities (*i.e.* high S_w), the $\rho_{c,meas}-\rho_{c,est}$ correlations
590 are good. Therefore, it is not possible to quantify water saturations accurately only by measuring
591 electrical resistivities. However, the accuracy is sufficient (especially for values close to S_w) to
592 highlight differences between the three treatment approaches (*i.e.* without and with enhancement).
593 Measurements allowed the distinction between four specific zones: S_{rw} zone, transition zone, S_m zone,
594 water zone.

595

596 **Acknowledgments**

597 This research was carried out as part of the SILPHES project supported by ADEME (French
598 Environment and Energy Management Agency) in the framework of the Future Investments
599 ("Investissements d'Avenir") funding scheme and the BRGM MULTISCALEXPER project. The
600 authors acknowledge ADEME and the BRGM/DEPA division for its financial support. The authors
601 also gratefully acknowledge the financial support provided to the PIVOTS project by the Centre – Val

602 de Loire region (ARD 2020 program and CPER 2015-2020) and the French Ministry of Higher
603 Education and Research (CPER 2015-2020 and public service subsidy to BRGM). Support from the
604 European Union via the European Regional Development Fund is also acknowledged. We thank
605 INOVYN for the assistance provided during the SILPHES project, in particular for providing access to
606 the Tavaux site.

607

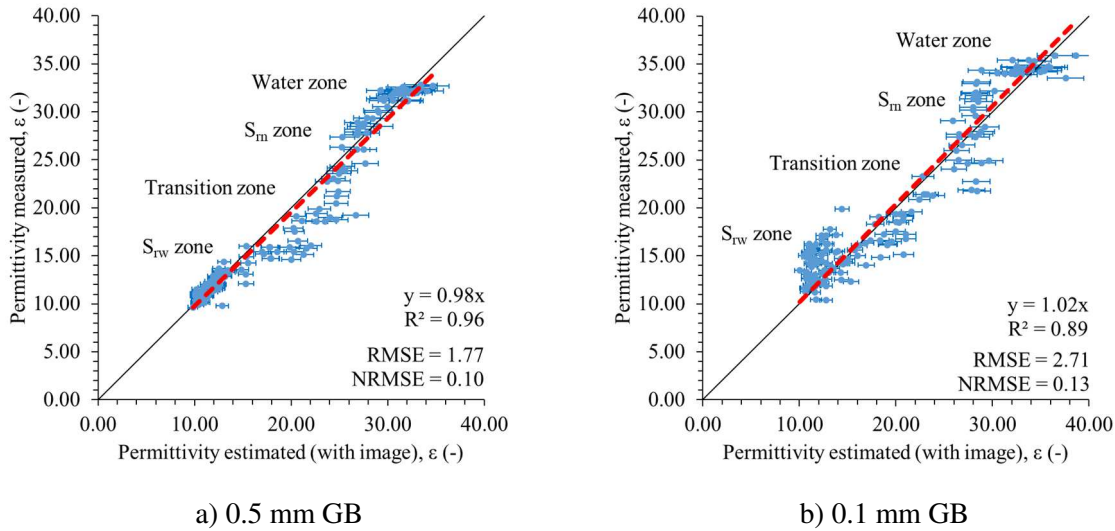
608

609 **Appendix**

610

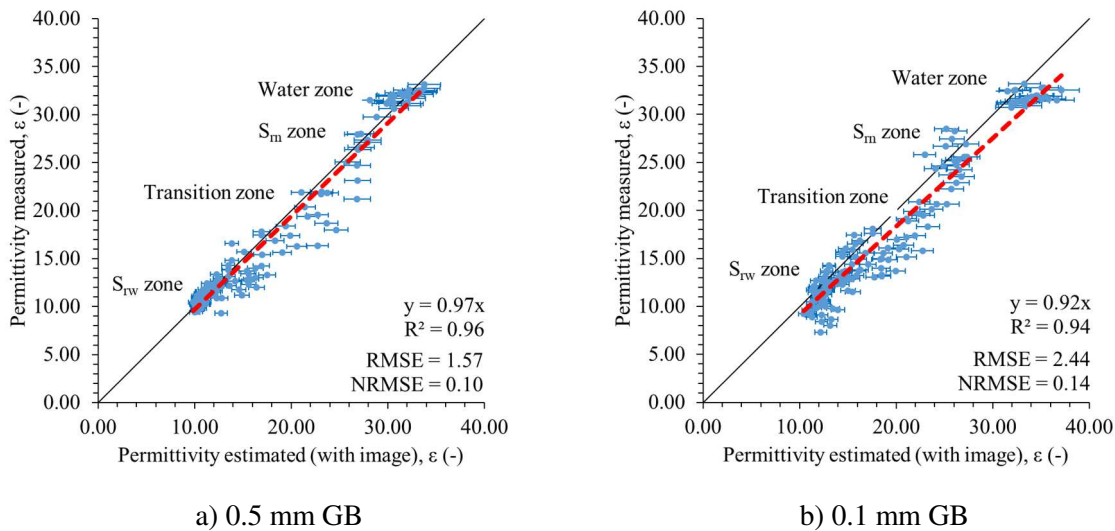
611 Figures 1A and 2A compare measured and estimated permittivity (with image interpretation) in the
 612 2D tank for 0.5 and 0.1 mm GB in the presence of chemical enhancement and with thermal
 613 enhancement, respectively.

614



615 Figure 1A: Comparison of measured and estimated permittivity (with image interpretation) in the 2D
 616 tank with a flow rate of 150 mL.min⁻¹ (with chemical enhancement) for a) 0.5 and b) 0.1 mm GB

617



618 Figure 2A: Comparison of measured and estimated permittivity (with image interpretation) in the 2D
 619 tank with a flow rate of 150 mL.min⁻¹ (with thermal enhancement) for a) 0.5 and b) 0.1 mm GB

620

621 Adding SDBS at its CMC has no effect on permittivity measurements; permittivities are therefore
622 estimated using Eq. 13. The NRMSE are 0.10 and 0.13 for 0.5 and 0.1 mm GB, respectively (Figure
623 1A). The NRMSE for the 0.5 mm GB is logically lower than those of the 0.1 mm GB.

624 Figure 2A compares measured and estimated permittivity (with image interpretation) in the 2D
625 tank for 0.5 and 0.1 mm GB and with thermal enhancement. The permittivity values were influenced
626 by temperature variations. The variations in ϵ_n and ϵ_w as a function of temperature were quantified and
627 integrated in the CRIM model (Eq. 13). These variations were estimated using Eq. 1A and Eq. 2A for
628 0.5 mm GB [Colombano et al. (2020)]:

$$\epsilon_n = 0.0367.T + 4.51 \quad \text{Eq. 1A}$$

$$\epsilon_w = 0.0231.T + 31.50 \quad \text{Eq. 2A}$$

629 where T ($^{\circ}\text{C}$) is the temperature in Celsius.

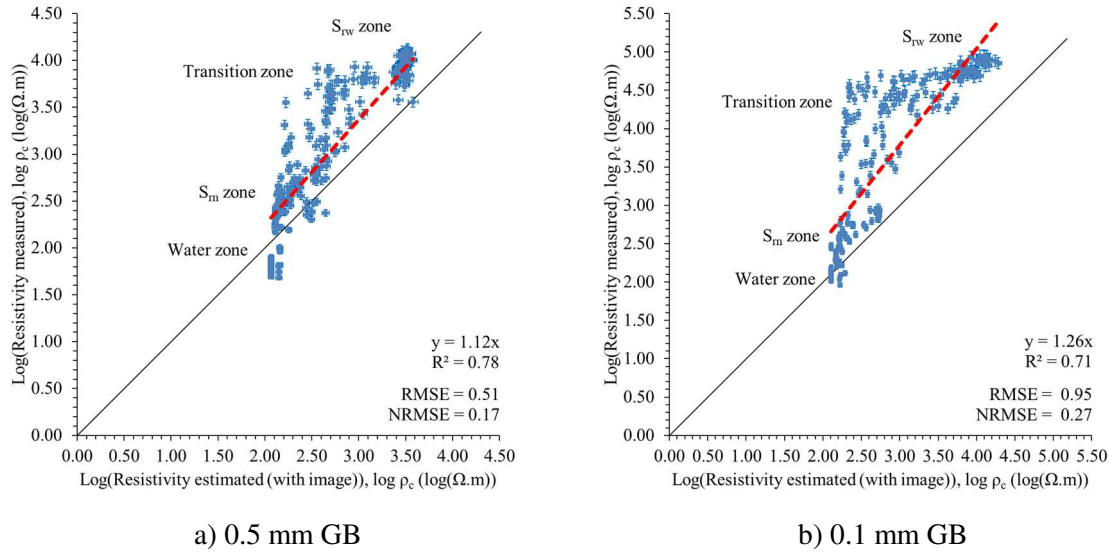
630 As shown in Figure 1A and Figure 2A, the NRMSE are between 0.10 and 0.14. The NRMSE for
631 the 0.5 mm GB are logically lower than those of the 0.1 mm GB (0.10 vs 0.14 for example for thermal
632 enhancement) because the fingering is more important. In the case of thermal and chemical
633 enhancements, four zones are clearly distinguished: S_{rw} zone, transition zone, S_m zone and water zone.
634 As stated above, in the transition zone the majority of the ϵ_{meas} were below ϵ_{est} .

635

636

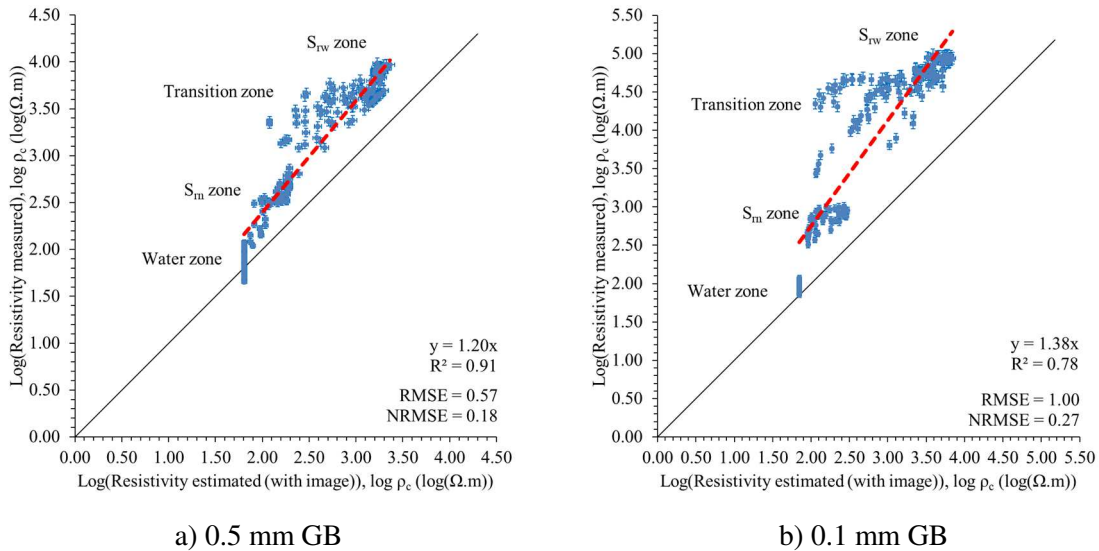
637 Figures 3A and 4A compare the measured and estimated resistivity (with image interpretation) in
 638 the 2D tank for 0.5 and 0.1 mm GB with chemical and thermal enhancements, respectively.

639



640 Figure 3A: Comparison of measured and estimated resistivity (with image interpretation) in the 2D
 641 tank with a flow rate of 150 mL.min⁻¹ (with chemical enhancement) for a) 0.5 and b) 0.1 mm GB

642



643 Figure 4A: Comparison of measured and estimated resistivity (with image interpretation) in the 2D
 644 tank with a flow rate of 150 mL.min⁻¹ (with thermal enhancement) for a) 0.5 and b) 0.1 mm GB

645

646 Adding SDBS at its CMC has a negligible impact on the measured electrical resistivities
 647 [Colombano et al. (2020)]. Eq. 14 was therefore considered to estimate the resistivity. The NRMSE

648 were 0.17 and 0.27 for 0.5 and 0.1 mm GB, respectively (Figure 3A), which means that the data
649 dispersivity is higher with the 0.1 mm GB. The $\rho_{c,meas}/\rho_{c,est}$ ratios for values close to S_{rw} are high: 3.20
650 and 5.99 for 0.5 and 0.1 mm GB, respectively.

651 Figure 4A compares the measured and estimated resistivity (with image interpretation) in the 2D
652 tank for 0.5 and 0.1 mm GB. The resistivity estimates were calculated by considering Eq. 14 and the
653 resistivity changes related to the increase in temperature. The increase in temperature results in an
654 increase in ionic mobility and a decrease in resistivities [Dakhnov (1962); Hayashi (2004); Light et al.
655 (2005); Grellier et al. (2008)]. The decrease in the resistivity of water and the DNAPL was determined
656 on the basis of experiments and the Dakhnov equation (Eq. 3A) [Colombano et al. (2020)]:

$$\rho_{c,f} = \frac{\rho_{c,f_0}}{1 + \alpha_{c,f}(T - T_0)} \quad \text{Eq. 3A}$$

657 where $\rho_{c,f}$ ($\Omega.m$) is the electrical resistivity of the fluid at temperature T ($^{\circ}C$), ρ_{c,f_0} ($\Omega.m$) is the
658 electrical resistivity of the fluid at temperature T_0 , and $\alpha_{c,w}$ ($^{\circ}C^{-1}$) is the temperature coefficient of
659 resistivity ($\alpha_{c,w} \approx 0.023$ $^{\circ}C^{-1}$ for $T_0=23$ $^{\circ}C$, and 0.025 $^{\circ}C^{-1}$ for $T_0=0$ $^{\circ}C$)

660 The NRMSE were 0.18 and 0.27 for 0.5 and 0.1 mm GB, respectively (Figure 3A). The
661 dispersivity was higher with 0.1 mm GB than with 0.5 mm GB. Here also, we note that the $\rho_{c,meas}/\rho_{c,est}$
662 ratios for values close to S_{rw} were high: 4.46 and 9.37 for 0.5 and 0.1 mm GB, respectively. As stated
663 above, we also distinguished four zones: S_{rw} zone, transition zone, S_m zone, water zone.

664

665

666

667 Notations

a_c	Empirical parameter	-
c_ε	Speed of light (velocity of electromagnetic waves) in vacuum	$m.s^{-1}$
K_g	Geometric coefficient	m
L_ε	Waveguide length	m
m_1, m_2	Cementation exponent of DNAPL and water phases	-
m_c	Cementing factor	-
R_e	Electrical resistance measured with SIP system using a reference liquid	Ω
S_n, S_w	DNAPL (non-wetting fluid) and water (wetting fluid) saturations	-
T	Temperature	$^\circ C$
t_ε	Travel time for the pulse to traverse the length of the embedded waveguide	s
v_i	Volume fraction of the i phase	-
$\alpha_{c,w}$	Temperature coefficient of resistivity	$^\circ C^{-1}$
α_ε	Empirical constant related to the geometry of the grains and their spatial distribution	-
$\varepsilon = \varepsilon_r$	Relative permittivity	-
ε_0	Free space permittivity	$F.m^{-1}$
ε_{air}	Relative permittivity of air measured at the beginning of the experiment	-
$\varepsilon_{air-theoretical}$	Theoretical relative permittivity of pure air ($\varepsilon_{air-theoretical}=1$)	-
ε'	Real dielectric permittivity	$F.m^{-1}$
ε_{est}	Effective relative permittivity of the medium estimated with the water saturation (based on image interpretation)	-
ε_i	Relative permittivity of the i phase	-
ε_{meas}	Effective relative permittivity of the medium measured	-
ε_n	Relative permittivity of DNAPL	-
ε_s	Relative permittivity of soil particles	-
ε_w	Relative permittivity of water	-
$\varepsilon_{w-theoretical}$	Relative permittivity of pure water ($\varepsilon_{w-theoretical}=80$ at $20^\circ C$)	-
ρ_c	Electrical resistivity of the bulk	$\Omega.m$
$\rho_{c,est}$	Electrical resistivity of the bulk estimated with the water saturation (based on image interpretation)	$\Omega.m$
$\rho_{c,f}$	Electrical resistivity of the fluid at temperature T	$\Omega.m$
$\rho_{c,f0}$	Electrical resistivity of the fluid at temperature T_0	$\Omega.m$
$\rho_{c,meas}$	Electrical resistivity measured of the bulk	$\Omega.m$
$\rho_{c,w}$	Electrical resistivity of the water at temperature T	$\Omega.m$
ρ_0	Measured resistivity value using a reference liquid	$\Omega.m$
$\sigma_{c,bulk} = \sigma_c$	Electrical conductivity of the bulk	$S.m^{-1}$
$\sigma_{c,DNAPL}$	Electrical conductivity of DNAPL	$S.m^{-1}$
$\sigma_{c,water}$	Electrical conductivity of water	$S.m^{-1}$
v_ε	Function of the propagation velocity	$m.s^{-1}$
\emptyset	Porosity	-

668

669

670 [Ajo-Franklin et al. (2004)] Ajo-Franklin, J., Geller, J. and Harris, J.: 2004, The dielectric
671 properties of granular media saturated with DNAPL/water mixtures, *Geophysical Research Letters*
672 **31**(L17501), 1–4.

673 [Archie (1942)] Archie, G.: 1942, The electrical resistivity log as an aid in determining some
674 reservoir characteristics, *Petroleum Transactions of AIME* **146**(1), 54–62.

675 [Arp and Hale (2019)] Arp, H. and Hale, S.: 2019, *REACH: Improvement of guidance and*
676 *methods for the identification and assessment of PMT/vPvM substances*, German Environment
677 Agency edn. 129 p.

678 [Bernabé et al. (2016)] Bernabé, Y., Li, M., Tang, Y. and Evans, B.: 2016, Pore space
679 connectivity and the transport properties of rocks, *Oil & Gas Science and Technology* **71**(4), 1–17.

680 [Bernabé et al. (2011)] Bernabé, Y., Zamora, M., Li, M., Mainault, A. and Tang, Y.: 2011,
681 Pore connectivity, permeability, and electrical formation factor: A new model and comparison to
682 experimental data, *Journal of Geophysical Research* **116**(B11204), 1–15.

683 [Birchak et al. (1974)] Birchak, J., Gardner, C., Hipp, J. and Victor, J.: 1974, High dielectric
684 constant microwave probes for sensing soil moisture, *Proceedings of the Institute of Electrical and*
685 *Electronics Engineers* **62**(1), 93– 98.

686 [Breede et al. (2011)] Breede, K., Kemna, A., Esser, O., Zimmermann, E., Vereecken, H.
687 and Huisman, J.: 2011, Joint measurement setup for determining spectral induced polarization and
688 soil hydraulic properties, *Vadose Zone Journal* **10**(2), 716–726.

689 [Brewster et al. (1995)] Brewster, M., Annan, A., Greenhouse, J., Kueper, B., Olhoeft, G.,
690 Redman, J. and Sander, K.: 1995, Observed migration of a controlled DNAPL release by
691 geophysical methods, *Ground Water* **33**, 987– 997.

692 [Brovelli and Cassiani (2011)] Brovelli, A. and Cassiani, G.: 2011, Combined estimation of
693 effective electrical conductivity and permittivity for soil monitoring, *Water Resources Research*
694 **47**(W08510).

695 [Brown et al. (2003)] Brown, S., Lesmes, D., Fourkas, G. and Sorenson, J.: 2003, Complex
696 Electrical Resistivity for Monitoring DNAPL Contamination - Final Technical Report, *Technical*
697 *Report 70012*, U.S. Department of Energy. 31 p.

698 [Brown et al. (2004)] Brown, S., Sorenson, J. and Brown, T.: 2004, A laboratory study of
699 the complex electrical resistivity response of soils, *In Symposium on the Application of*
700 *Geophysics to Engineering and Environmental Problems 2004*, Society of Exploration
701 Geophysicists, pp. 528–539.

702 [Brusseau et al. (2006)] Brusseau, M., Peng, S., Schnaar, G. and Costanza-Robinson, M.:
703 2006, Relationships among air-water interfacial area, capillary pressure, and water saturation for a
704 sandy porous medium, *Water Resources Research* **42**(W03501).

705 [Byun et al. (2019)] Byun, Y., Hong, W. and Yoon, H.: 2019, Characterization of cementation
706 factor of unconsolidated granular materials through time domain reflectometry with variable
707 saturated conditions, *Materials* **12**(8), 1340–1354.

708 [Cai et al. (2017)] Cai, J., Wei, W., Hu, X. and Wood, D.: 2017, Electrical conductivity models
709 in saturated porous media: A review, *Earth-Science Reviews* **171**, 419–433.

710 [Capparelli et al. (2018)] Capparelli, G., Spolverino, G. and Greco, R.: 2018, Experimental
711 Determination of TDR Calibration Relationship for Pyroclastic Ashes of Campania (Italy),
712 *Sensors* **18**(3727), 1–14.

713 [Cardarelli and Di Filippo (2009)] Cardarelli, E. and Di Filippo, G.: 2009, Electrical resistivity
714 and induced polarization tomography in identifying the plume of chlorinated hydrocarbons in
715 sedimentary formation: a case study in (Milan-Italy), *Waste Management and Research*
716 **27**(6), 595–602.

717 [Cazaux et al. (2014)] Cazaux, D., Colombano, S., Joubert, A., Dumestre, A. and Lecuelle,
718 G.: 2014, Optimized physical recovery of DNAPL using upwelling technique and geostatistical
719 analysis at large field scale, *Ninth International Conference on Remediation of Chlorinated and*
720 *Recaclitrant Compounds*, number A1, Battelle Press, Columbus, OH, USA, Monterey, CA, USA,
721 p. 5.

722 [Chambers et al. (2004)] Chambers, J., Loke, M., Ogilvy, R. and Meldrum, P.: 2004,
723 Noninvasive monitoring of DNAPL migration through a saturated porous medium using electrical
724 impedance tomography, *Journal of Contaminant Hydrology* **68**(1–2), 1–22.

725 [Cohen and Mercer (1993)] Cohen, R. and Mercer, J.: 1993, DNAPL Site Evaluation, *Technical*
726 *Report EPA/600/R-93/022*, Edited by USEPA Office of Research and Development. 369 p.

727 [Colombano (2019)] Colombano, S.: 2019, *Improvement of the recovery of heavy*
728 *chlorinated organic compounds in saturated porous media by thermal and chemical*
729 *enhancements: experimental and two-phase flow modeling approaches*, PhD thesis, Paris, France.
730 480 p.

731 [Colombano et al. (2020)] Colombano, S., Davarzani, H., van Hullebusch, E., Huguenot, D.,
732 Guyonnet, D., Deparis, J. and Ignatiadis, I.: 2020, Thermal and chemical enhanced recovery of
733 heavy chlorinated organic compounds in saturated porous media: 1D cell drainage-imbibition
734 experiments, *Science of the Total Environment* **706**(135758).

735 [Colombano et al. (2021)] Colombano, S., Davarzani, H., van Hullebusch, E., Huguenot, D.,
736 Guyonnet, D., Deparis, J., Lion, F. and Ignatiadis, I.: 2021, Comparison of thermal and chemical
737 enhanced recovery of DNAPL in saturated porous media: 2D tank pumping experiments and two-
738 phase flow modelling, *Science of the Total Environment* **760**(143958).

739 [Constable and Srnka (2007)] Constable, S. and Srnka, L.: 2007, An introduction to marine
740 controlled-source electromagnetic methods for hydrocarbon exploration, *Geophysics* **72**(2), WA3–
741 WA12.

742 [Dakhnov (1962)] Dakhnov, V.: 1962, *Geophysical well logging*, number 57-2, Q. Colorado
743 School of Mines. 445 p.

744 [Dasberg and Hopmans (1992)] Dasberg, S. and Hopmans, J.: 1992, Time domain
745 reflectometry calibration for uniformly and nonuniformly wetted sandy and clayey loam soils, *Soil*
746 *Science Society of America Journal* **56**(5), 1341–1345.

747 [Deng et al. (2017)] Deng, Y., Shi, X., Xu, H., Sun, Y., Wu, J. and Revil, A.: 2017, Quantitative
748 assessment of electrical resistivity tomography for monitoring DNAPLs migration – Comparison
749 with high-resolution light transmission visualization in laboratory sandbox, *Journal of Hydrology*
750 **544**, 254–266.

751 [Deparis et al. (2019)] Deparis, J., Joubert, A., Francois, B., Nodot, E., Invernizzi, T.,
752 Iravani, A., Dumestre, A., Fatin-Rouge, N., Maire, J., Kaifas, D., Triger, A., Klein, P., Giraud, Q.,

753 Paris, B., Cazaux, D., Gourry, J., Davarzani, H. and Colombano, S.: 2019, On the use of
754 Geophysical measurements to monitored DNAPL extraction, *AquaConSoil 2019, 15th*
755 *International Conference*, Antwerp, Belgium.

756 [Dirksen and Dasberg (1993)] Dirksen, C. and Dasberg, S.: 1993, Improved calibration of
757 time domain reflectometry soil water content measurements, *Soil Science Society of America*
758 *Journal* **57**(3), 660–667.

759 [Dobson et al. (1985)] Dobson, M., Ulaby, F., Hallikainen, M. and El-Rayes, M.: 1985,
760 Microwave dielectric behaviour of wet soil, part ii, dielectric mixing models, *Institute of Electrical*
761 *and Electronics Engineers Transactions on Geoscience and Remote Sensing* **23**, 35–46.

762 [Endres and Knight (1992)] Endres, A. and Knight, R.: 1992, A theoretical treatment of the effect
763 of microscopic fluid distribution on the dielectric properties of partially saturated rocks,
764 *Geophysical Prospecting* **40**(3), 307–324.

765 [Falta et al. (2005b)] Falta, R., Basu, N. and Rao, P.: 2005b, Assessing impacts of partial
766 mass depletion in DNAPL source zones: II. Coupling source strength functions to plume
767 evolution, *Journal of Contaminant Hydrology* **79**(1-2), 45–66.

768 [Friedman (2005)] Friedman, S.: 2005, Soil properties influencing apparent electrical
769 conductivity: a review, *Computers and electronics in agriculture* **46**(1-3), 45–70.

770 [Ghanbarian and Sahimi (2017)] Ghanbarian, B. and Sahimi, M.: 2017, Electrical conductivity
771 of partially saturated packings of particles, *Transport in Porous Media* **118**(1), 1–16.

772 [Glover (2010)] Glover, P.: 2010, A generalised archie's law for n phases, *Geophysics*
773 **6**, E247–E265.

774 [Grellier et al. (2008)] Grellier, S., Guérin, R., Robain, H., Bobachev, A., Vermeersch, F. and
775 Tabbagh, A.: 2008, Monitoring of leachate recirculation in a bioreactor landfill by 2-d electrical
776 resistivity imaging, *Journal of Environmental and Engineering Geophysics* **13**(4), 351–359.

777 [Han et al. (2015)] Han, T., Best, A., Sothcott, J., North, L. and MacGregor, L.: 2015,
778 Relationships among low frequency (2 hz) electrical resistivity, porosity, clay content and
779 permeability in reservoir sandstones, *Journal of Applied Geophysics* **112**, 279–289.

780 [Hayashi (2004)] Hayashi, M.: 2004, Temperature-electrical conductivity relation of water for
781 environmental monitoring and geophysical data inversion, *Environmental Monitoring and*
782 *Assessment* **96**(1-3), 119–128.

783 [IARC (2018)] IARC: 2018. <https://www.iarc.fr/>

784 [Iravani et al. (2020a)] Iravani, M., Deparis, J., Davarzani, H., Colombano, S., Guérin, R. and
785 Maineult, A.: 2020a, The influence of temperature on the dielectric permittivity and complex
786 electrical resistivity of porous media saturated with DNAPLs: A laboratory study, *Journal of*
787 *Applied Geophysics* **172**, 103921.

788 [Iravani et al. (2020b)] Iravani, M., Deparis, J., Davarzani, H., Colombano, S., Guérin, R. and
789 Maineult, A.: 2020b, Complex electrical resistivity and dielectric permittivity responses to dense
790 non-aqueous phase liquids imbibition and drainage in porous media: a laboratory study,
791 *Geophysical Prospecting* p. accepted.

792 [ITRC (2002)] ITRC: 2002, *DNAPL Source Reduction: Facing the Challenge*,
793 Technical/Regulatory Guidelines, Interstate Technology & Regulatory Council, Washington, DC,
794 USA. 40 p.

795 [Jougnot et al. (2018)] Jougnot, D., Jiménez-Martínez, J., Legendre, R., Le Borgne, T.,
796 Méheust, Y. and Linde, N.: 2018, Impact of small-scale saline tracer heterogeneity on electrical
797 resistivity monitoring in fully and partially saturated porous media: Insights from geoelectrical
798 milli-fluidic experiments, *Advances in Water Resources* **113**, 295–309.

799 [Kamona et al. (2003)] Kamona, M., Endob, K. and Katsumi, T.: 2003, Measuring the k-S-p
800 relations on DNAPLs migration, *Engineering Geology* **70**, 351 – 363.

801 [Kargas and Soulis (2012)] Kargas, G. and Soulis, K.: 2012, Performance analysis and calibration
802 of a new low-cost capacitance soil moisture sensor, *Journal of Irrigation and Drainage*
803 *Engineering* **138**(7), 632–641.

804 [Kueper et al. (2003)] Kueper, B., Wealthall, G., Smith, J., Leharne, S. and Lerner, D.: 2003,
805 *An illustrated handbook of DNAPL transport and fate in the subsurface*, number 1844320669,
806 U.K. Environment Agency, Bristol, England, United Kingdom. 67 p.

807 [Laloy et al. (2011)] Laloy, E., Javaux, M., Vanclooster, M., Roisin, C. and Biielders, C.:
808 2011, Electrical resistivity in a loamy soil: Identification of the appropriate pedo-electrical model,
809 *Vadose Zone Journal* **10**(3), 1023–1033.

810 [Li et al. (2015)] Li, M., Tang, Y., Bernabé, Y., Zhao, J., Li, X., Bai, X. and Zhang, L.: 2015,
811 Pore connectivity, electrical conductivity, and partial water saturation: Network simulations,
812 *Journal of Geophysical Research: Solid Earth* **120**(6), 4055–4068.

813 [Light et al. (2005)] Light, T., Licht, S., Bevilacqua, A. and Morashc, K.: 2005, The fundamental
814 conductivity and resistivity of water, *Electrochemical and Solid-State Letters* **8**(1), E16–E19.

815 [Linde et al. (2006)] Linde, N., Binley, A., Tryggvason, A., Pedersen, L. and Revil, A.:
816 2006, Improved hydrogeophysical characterization using joint inversion of cross-hole electrical
817 resistance and ground-penetrating radar traveltime data, *Water Resources Research* **42**(W12404).

818 [Linde et al. (2007)] Linde, N., Jougnot, D., Revil, A., Matthäi, S., Arora, T., Renard, D.
819 and Doussan, C.: 2007, Streaming current generation in two-phase flow conditions, *Geophysical*
820 *Research Letters* **34**(L03306).

821 [Maineult et al. (2004)] Maineult, A., Bernabé, Y. and Ackerer, P.: 2004, Electrical response
822 of flow, diffusion, and advection in a laboratory sand box, *Vadose Zone Journal* **3**(4), 1180–1192.

823 [Maire et al. (2018)] Maire, J., Joubert, A., Kaifas, D., Invernizzi, T., Mardue, J.,
824 Colombano, S., Cazaux, D., Marion, C., Klein, P., Dumestre, A. and Fatin-Rouge, N.: 2018a,
825 Assessment of flushing methods for the removal of heavy chlorinated compounds DNAPL in an
826 alluvial aquifer, *Science of the Total Environment* (612), 1149–1158.

827 [McGuire et al. (2006)] McGuire, T., McDade, J. and Newell, C.: 2006, Performance of
828 DNAPL Source Depletion Technologies at 59 Chlorinated Solvent-Impacted Sites, *Ground Water*
829 *Monitoring and Remediation* **26**(1), 73–84.

830 [NIEHS (2015)] NIEHS: 2015, Chlorinated organics – information page, website.
831 http://tools.niehs.nih.gov/srp/research/research4_s3_s4.cfm

832 [Noel (2014)] Noel, C.: 2014, *Suivi de la biodégradation des hydrocarbures par le couplage*
833 *des mesures géophysiques électriques du sol (polarisation provoquée) et des analyses des gaz*

834 (*concentration du CO2 et isotopie du carbone*), PhD thesis, Université d'Orléans, Orléans, France.
835 256 p.

836 [Noel et al. (2016a)] Noel, C., Gourry, J., Deparis, J., Blessing, M., Ignatiadis, I. and
837 Guimbaud, C.: 2016a, Combining geoelectrical measurements and CO2 analyses to monitor the
838 enhanced bioremediation of hydrocarbon-contaminated soils: a field implementation, *Applied and*
839 *Environmental Soil Science* **2016**, 1–15.

840 [Noel et al. (2016b)] Noel, C., Gourry, J., Deparis, J., Ignatiadis, I., Battaglia-Brunet, F. and
841 Guimbaud, C.: 2016b, Suitable real-time monitoring of the aerobic biodegradation of toluene in
842 contaminated sand by spectral induced polarization measurements and CO2 analyses, *Near*
843 *Surface Geophysics* **14**(3), 263–273.

844 [Nyquist et al. (1999)] Nyquist, J., Carr, B. and Davis, R.: 1999, DC resistivity monitoring of
845 potassium permanganate injected to oxidize TCE in situ, *Journal of Environmental and*
846 *Engineering Geophysics* **4**(3), 135–147.

847 [Persson and Berndtsson (2002)] Persson, M. and Berndtsson, R.: 2002, Measuring nonaqueous
848 phase liquid saturation in soil using time domain reflectometry, *Water Resources Research*
849 **38**(5), 22.1–22.8.

850 [Philippe et al. (2020)] Philippe, N., Davarzani, H., Colombano, S., Dierick, M., Klein, P. and
851 Marcoux, M.: 2020, Experimental study of the temperature effect on two-phase flow properties in
852 highly permeable porous media: Application to the remediation of dense non-aqueous phase
853 liquids (DNAPLs) in polluted soil, *Advances in Water Resources* **146**(103783).

854 [Power et al. (2014)] Power, C., Gerhard, J., Karaoulis, M., Tsourlos, P. and Giannopoulos,
855 A.: 2014, Evaluating four-dimensional time-lapse electrical resistivity tomography for monitoring
856 DNAPL source zone remediation, *Journal of Contaminant Hydrology* **162**, 27–46.

857 [Redman and DeRyck (1994)] Redman, J. and DeRyck, S.: 1994, Monitoring non-aqueous
858 phase liquids in the subsurface with multilevel time domain reflectometry probes, *Proceedings of*
859 *the Symposium on Time Domain Reflectometry in Environmental, Infrastructure, and Mining*
860 *Applications*, Spec. Publ. SP, .NTIS PB95-105789, 19-94, U.S. Bur. of Mines, Washington, D.C.,
861 USA, p. 207– 215.

862 [Redman et al. (1991)] Redman, J., Kueper, B. and Annan, A.: 1991, Dielectric stratigraphy
863 of a DNAPL spill and implications for detection with ground penetrating radar, *Aquifer*
864 *Restoration, Ground Water Monitoring and Geophysical Methods, 5th National Outdoor Action*
865 *Conference*, Natl. Ground Water Assoc., Las Vegas, NV., USA.

866 [Revil (2012)] Revil, A.: 2012, Spectral induced polarization of shaly sands: influence of the
867 electrical double layer, *Water Resources Research* **48**(2), 1–23.

868 [Revil (2017)] Revil, A.: 2017, Transport of water and ions in partially water-saturated
869 porous media. Part 1. Constitutive equations, *Advances in Water Resources* **103**, 119–138.

870 [Reynolds (2011)] Reynolds, J.: 2011, *An Introduction to Applied and Environmental*
871 *Geophysics*, number 978-0-471-48535-3, 2nd edition edn, Wiley-Blackwell, Chichester, UK. 710
872 p.

873 [Árnason et al. (2000)] Árnason, K., Karlsdóttir, R., Eysteinnsson, H., Flóvenz, O. and
874 Gudlaugsson, S.: 2000, The resistivity structure of high-temperature geothermal systems in
875 iceland, *Proceedings of the World Geothermal Congress 2000*, Kyushu-Tohoku, Japan, pp. 923–
876 928.

877 [Roth et al. (1990)] Roth, K., Schulin, R., Fluhler, H. and Attinger, W.: 1990, Calibration of time
878 domain reflectometry for water content measurements using a composite dielectric approach,
879 *Water Resources Research* **26**, 2267–2273.

880 [Schmutz et al. (2010)] Schmutz, M., Revil, A., Vaudelet, P., Batzle, M., Femenia Viñao, P.
881 and Werkema, D.: 2010, Influence of oil saturation upon spectral induced polarization of oil-
882 bearing sands, *Geophysical Journal International* **183**, 211–224.

883 [Smallwood (2012)] Smallwood, I.: 2012, *Handbook of organic solvent properties*,
884 Butterworth-Heinemann, Oxford, UK. 306 p.

885 [Sogade et al. (2006)] Sogade, J., Scira-Scappuzzo, F., Vichabian, Y., Shi, W., Rodi, W.,
886 Lesmes, D. and Morgan, F.: 2006, Induced-polarization detection and mapping of contaminant
887 plumes, *Geophysics* **71**(3), B75–B84.

888 [Topp et al. (1980)] Topp, G., Davis, J. and Annan, A.: 1980, Electromagnetics determination of
889 soil water content: Measurements in coaxial transmission lines, *Water Resources Research*
890 **16**, 574–582.

891 [Winsauer et al. (1952)] Winsauer, W., Shearin, H., Masson, P. and Williams, M.: 1952,
892 Resistivity of brine-saturated sands in relation to pore geometry, *American Association of*
893 *Petroleum Geologists Bulletin* **36**(2), 253–277.

894